8-15-2021

Three-Dimensional Phase Field Modeling of Fracture in Shape Memory Ceramics

Ehsan Moshkelgosha
Boise State University

Mahmood Mamivand
Boise State University

Publication Information

Moshkelgosha, Ehsan and Mamivand, Mahmood. (2021). "Three-Dimensional Phase Field Modeling of Fracture in Shape Memory Ceramics". *International Journal of Mechanical Sciences, 204*, 106550. https://doi.org/10.1016/j.ijmecsci.2021.106550

Three-Dimensional Phase Field Modeling of Fracture in Shape Memory Ceramics

Ehsan Moshkelgosha
Micron School of Materials Science and Engineering
Boise State University
Boise, ID, USA

Mahmood Mamivand
Department of Mechanical and Biomedical Engineering
Boise State University
Boise, ID, USA

Abstract

Despite the vast applications of transformable ceramics, such as zirconia-based ceramics, in different areas from biomedical to aerospace, the fundamental knowledge about their mechanical degradation procedure is limited. The interaction of the phase transformation and crack growth is crucial as the essential underlying mechanism in fracture of these transformable ceramics, also known as shape memory ceramics. This study develops a three-dimensional (3D) multiphysics model that couples the variational formulation of brittle crack growth to the Ginzburg-Landau equations of martensitic transformation. We parameterized the model for the 3D single crystal zirconia, which experienced stress- and thermal-induced tetragonal to monoclinic transformation. The developed 3D model considers all 12 monoclinic variants, making it possible to acquire realistic microstructures. Surface uplifting, self-accommodated martensite pairs formation, and transformed zone fragmentation were observed by the model, which agrees with the experimental observations. The influence of the crystal lattice orientation is investigated in this study, which reveals its profound effects on the transformation toughening and crack propagation path.

Keywords: shape memory ceramics, three-dimensional modeling, crack growth, phase field modeling, martensitic transformation, zirconia

1. Introduction

Shape memory ceramics (SMCs) are excellent choices for actuators, especially in high temperature and corrosive applications. In particular, the zirconia-based ceramics with the combination of superior qualities like high strength and low thermal conductivity are promising choices among the other shape memory ceramics for a vast range of applications from biomedical implants to thermal barrier coatings on turbine blades in jet engines [1].

Garvie et al. [2] were the first who showed that it is possible to gain a significant increase in zirconia strength by making the tetragonal phase stable at room temperature. Tetragonal stabilization is feasible by adding oxide dopants or reducing the grain sizes. Both techniques reduce the tetragonal to monoclinic transformation temperature by decreasing the transformation deriving force.

The stabilized zirconia is resistant to crack propagation, as the stress concentration at the crack tip excites the tetragonal to monoclinic ($t \rightarrow m$) transformation. This transformation results in a considerable shear (0.16) and volume expansion (0.04) that will create a domain with large compressive stresses leading to crack tip closure and preventing the crack growth, which enhances the toughening property of zirconia [3].

Despite the superior properties of zirconia, such as applicability for a wider range of temperatures and higher energy absorption, compared to the metallic shape memory materials [4], their widespread application is limited due to their brittleness and low fatigue life. While recent studies [4] have shown that increasing the fatigue life is possible by reducing the sample size, we still lack the fundamental knowledge of how martensitic transformation (MT) and crack interact concurrently, in particular in three-dimensional (3D) domains.

Fracture of zirconia has been the subject of numerous experimental studies [5–10]. Some of the two-dimensional (2D) experimental studies such as X-ray diffraction [11], transmission electron microscopy [12], optical microscopy [13], scanning electron microscopy, and neutron powder diffraction [14] have revealed fundamental knowledge on the crack and MT interaction. However, some information is missed in 2D. Fortunately, 3D observation of crack formation and propagation in shape memory ceramics has become possible by using Atomic Force Microscopy (AFM). Deville et al. [15] showed that AFM could successfully be used to observe ceria-stabilized zirconia transformation toughening and how the stress in the field around the propagating cracks leads to $t \rightarrow m$ transformation. Deville et al. [15] used a high resolution AFM to examine the development of self-accommodated martensite pairs around the crack zones at the surface of the samples. However, while AFM provides some 3D information for the transformation toughening in zirconia, there are some limitations associated with the AFM technique, for example, AFM only gives the in-surface information and we are missing in-bulk information.

Alongside with the experimental studies, theoretical studies and simulations can also advance the fundamental knowledge of crack growth interaction with the MT. Fracture and transformation toughening mechanisms in transformable brittle materials was investigated at macroscale by numerous studies in the past years [16–21]. To find the features and mechanisms involved in transformation toughening in transformable brittle materials, Evans and Cannon [22] provided an inclusive study that reveals the effect of microstructure and materials chemistry on transformation toughening. A comprehensive review on this subject has been conducted by Hannink et al. [3] and Kelly and Rose [23]. In early studies, two strategies were used to calculate the amount of toughening caused by the transformation. The first one used the concept of linear elastic fracture mechanics to estimate the phase transformation's shielding effect [16], while the other one determined the fracture energy that was originating from the phase transformation associated with a growing crack [17].

Although classical models and studies revealed some underlying features and mechanisms regarding the transformation toughening, they could not consider the dynamic interaction of crack propagation and MT simultaneously. Moreover, the classical models were not capable of considering microstructure discontinuities such as grain boundaries, inclusions, second phases, etc., and microstructure features like grain size, which influence the SMCs properties and impact the MT effectiveness [24]. In brief, the classical models lacked in considering several mechanisms such as crack deflection, crack bridging, microcracks formation, different conditions like environment, or stress state, which have intense effects on the fracture of SMCs [24].

Some models have been developed to predict the role of transformation toughening and reverse transformation on crack propagation in shape memory materials [25–28]. While important insight has been gained, these efforts have been restricted to discrete numerical methods, such as cohesive zone formulations. Discrete numerical methods for fracture are limited when dealing with the complex conditions of practical applications and, consequently, important challenges remain unaddressed (crack nucleation, mixed-mode, interacting cracks, etc.). Moreover, to the best of the authors' knowledge, a modeling framework capable of explicitly predicting crack growth behavior in shape memory materials considering the microstructure evolution such as the competition between the different martensite variants has not been presented yet.

Toward the concurrent modeling of MT and crack growth, some recent works have been primarily limited in 2D. Zhao et al. [29] and Zhu and Luo [30] have investigated the crack growth in zirconia by employing the phase field (PF) model of Mamivand et al. [31–33] for $t \rightarrow m$ transformation accompanied by the Ginzburg-Landau formalism for the crack propagation [34–39]. Their studies lacked predicting the experimentally observed crack deflection and intergranular crack growth, which is common in doped zirconia [40]. We have recently developed 2D PF models for fracture in single crystal and polycrystalline zirconia [41–43]. In these studies, we proposed an anisotropic PF model that couples the Ginzburg Landau formulation of $t \rightarrow m$ transformation to the Griffith's variational framework of fracture. The models successfully predicted the crack nucleation, propagation, and branching behavior and explained the experimentally observed abnormal crack growth patterns in both single crystal and polycrystalline zirconia. However, all these models are limited to 2D and consider only 2 variants of the monoclinic phase, while in 3D, the monoclinic phase can have 12 variants.

To surpass the deficiency of the classical and 2D fracture models for SMCs and enhance the current knowledge of SMCs degradation, in this work, for the first time, we present a 3D model that captures the concurrent co-evolution of crack and MT in the transformable materials. This model is based on the PF method, which has proven to be a robust technique for modeling moving boundary problems. We couple two separate physics, i.e., MT and crack growth, via two well-established and validated PF models.

Regarding the phase transformation part, the PF method has become a trustworthy technique for the solid-state phase transformations [44,45]. The PF technique can consider all aspects of the phase transformation, including crystallography, thermodynamics, and kinetics [46]. Studies have shown the phase field method's capabilities in modeling different phase transformation problems, such as solidification [47,48] and solid-state phase transformation [49–52]. Specifically, the PF modeling of MT was fundamentally driven by Khachaturyan, Wang, and Chen [53,54], and it was initially based on Khachaturyan's microelasticity theory and time dependent Ginzburg–Landau kinetic formalism. Mamivand et al. [55] provided a comprehensive review for various types of PF models for MT. The phase field was used to model different forms of MT, like cubic to tetragonal [56,57], hexagonal to orthorhombic [58–60], cubic to monoclinic [61], and tetragonal to monoclinic [23,62–64] transformations.

For the crack side of the problem, several studies [65–69] have used the PF method for crack growth modeling due to its robust performance and timely implementation. The smooth transition from the cracked to the intact domain in the PF method is feasible using a scalar field called the PF variable. Using the PF variable, the crack is no longer a discontinuity, which provides a diffuse interface for the crack that enables predicting the crack nucleation, growth, and branching efficiently in complex geometries. Moreover, the straight coupling of fracture framework to other physics like MT is a plus for the PF modeling of crack growth.

In this paper, we present an elastically anisotropic and inhomogeneous 3D PF model for co-evolution of $t \rightarrow m$ transformation and crack propagation in zirconia. Unlike the 2D models, the 3D formalism empowers us to consider all possible monoclinic variants, and consequently, obtain more realistic results.

The paper outline is as follows. In section 2, we provide a brief description of the crystallography of $t \rightarrow m$ transformation in zirconia and then explain the PF equations for MT and fracture and their coupling. In section 3, we validate the model by comparing the results with the experimental observations. Then we elaborate the temporal and spatial evolution of simultaneous fracture and MT in 3D and study the influence of lattice orientation on the fracture, crack pattern, and toughening in 3D zirconia single crystal. Finally, the key findings are summarized in section 4.

2. Method

2.1. Phase Field Modeling of $t \rightarrow m$ Transformation in Zirconia

In this study, the PF model of MT is based on the experimentally validated model developed originally by Mamivand et al. [32,33,64,70]. In the PF modeling of MT, the PF variables, also known as order parameters, are responsible for describing the smooth transition from $t \rightarrow m$ in microstructural domain. PF variables in MT are the possible martensite phase variants, which is monoclinic in this study.

Order parameter $\eta_p(\vec{r},t)$ is applied to describe the p^{th} monoclinic variant, where t represents the time and r is the position vector. The value of η_p varies from 0 to 1 during the MT. The p^{th} monoclinic phase exists when $\eta_p = 1$, and when $\eta_p = 0$, the domain is either the parent tetragonal phase or one of the other monoclinic variants. Below we briefly describe these variants and refer the interested readers to Ref. [70] for more details.

2.1.1. Crystallography of Tetragonal to Monoclinic Transformation in Zirconia

Monoclinic variants, that are derived from tetragonal, are categorized into three main correspondences, namely correspondence *A*, *B*, and *C*. These correspondences are defined based on the monoclinic axis that is derived from the c_t (axis *c* in tetragonal). For example, correspondence *A* indicates that c_t becomes a_m (axis *a* in monoclinic). However, we need a more comprehensive notation as in the case of correspondence *A*, a_t and b_t have this chance to become either b_m or c_m. Therefore, in this paper, we use the Hayakawa et al. [13,71,72] notation system to identify all monoclinic variants. This notation technique uses a three-letter-sign for each monoclinic variant. If we consider a_t, b_t and c_t as the tetragonal axes and a_m, b_m and c_m as the monoclinic axes, the three letters in Hayakawa's notation, from left to right, show which monoclinic axes are derived from a_t, b_t, and c_t. For instance, *BCA* variant indicates

that b_m is derived from a_t, c_m is derived from b_t, and a_m is derived from c_t. The angles between a_m and c_m in monoclinic phase is about 99° [23]. Therefore, there are two possible orientations for each monoclinic variant, *OR1*, and *OR2*. *OR1* (*OR2*) indicates that a_m (c_m) is aligned with its correspondent axis in tetragonal and c_m (a_m) is tilted. Figure 1 demonstrates four possible monoclinic variants of the correspondence *C*.

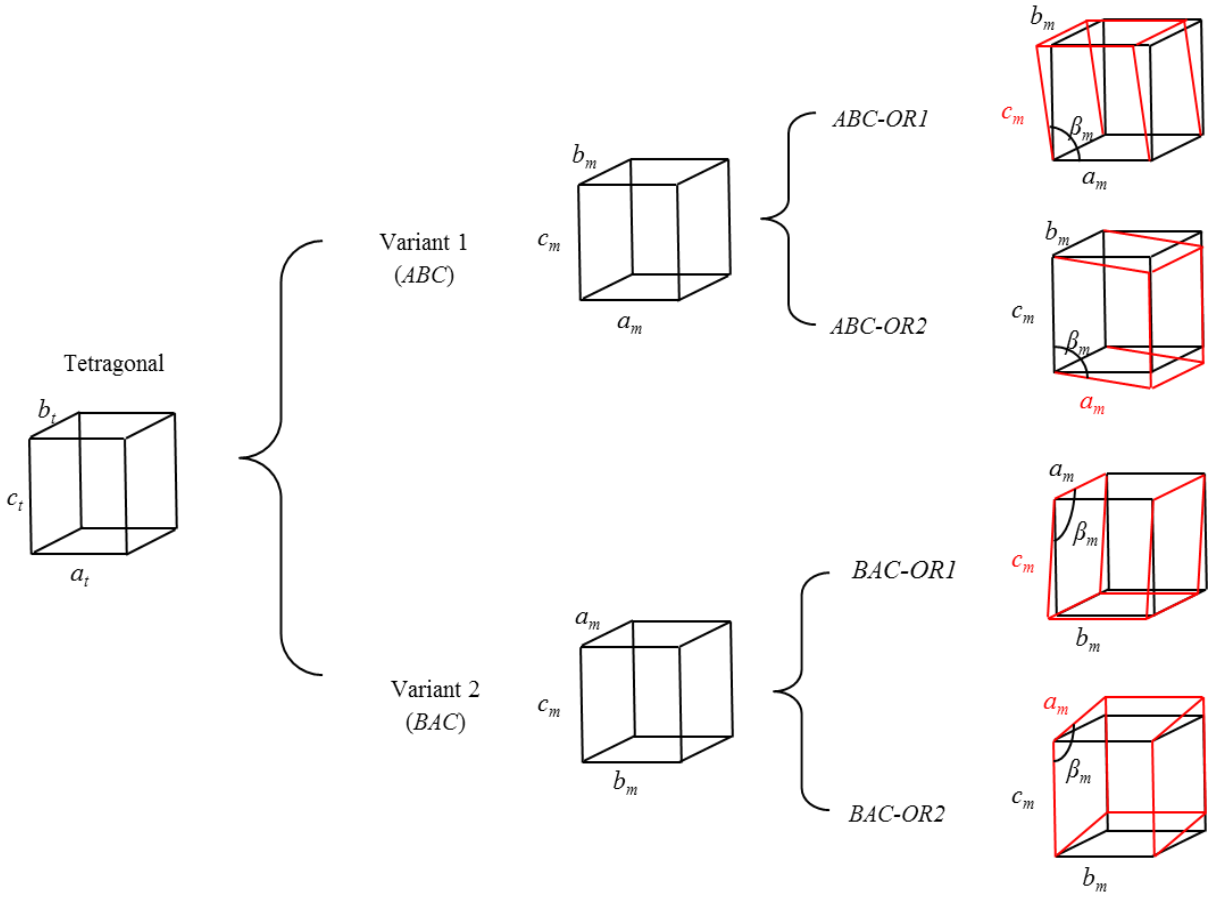

Figure 1. Schematic representation of possible monoclinic variants derived from the correspondence C, i.e., c_t become c_m [70].

In the $t \rightarrow m$ transformation, the incorporation of orientations, variants, and correspondences leads to 12 feasible monoclinic crystals for each tetragonal crystal. Figure 2 shows the monoclinic correspondences, orientations, variants, and their self-accommodating variants in $t \rightarrow m$ transformation.

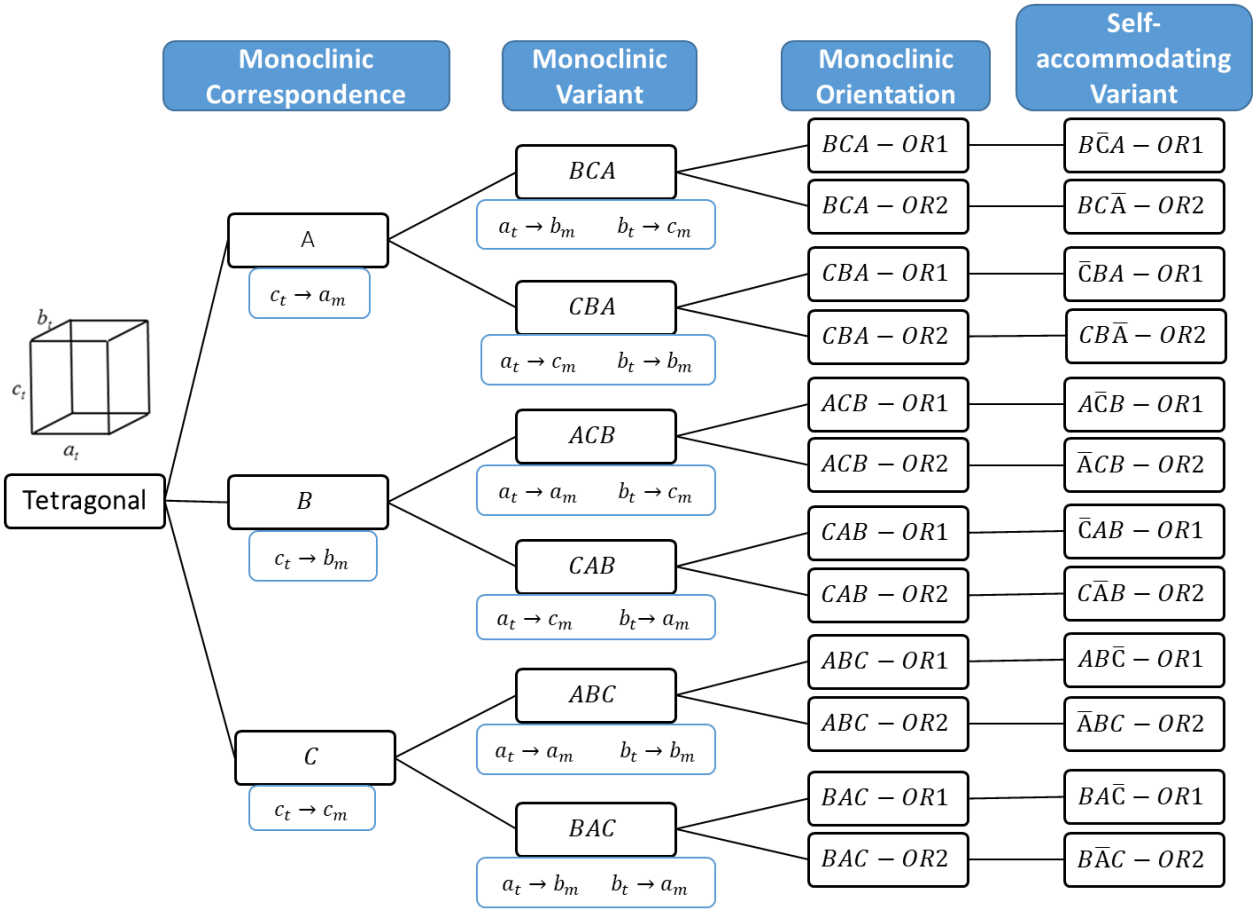

Figure 2. The feasible monoclinic variants and their self-accommodating variants in $t \to m$ transformation [70].

2.1.2. Phase Field Modeling of Tetragonal to Monoclinic Transformation

As mentioned above, in the PF modeling of MT the order parameters are martensite, here monoclinic, variants. Since these variants are not conserved quantities, the Ginzburg–Landau [73] formalism is appropriate for the PF framework. The Ginzburg–Landau equation is used for the evolution of PF variables in MT in the form of the following equation:

$$\frac{\partial \eta_p(\vec{r},t)}{\partial t} = -L\frac{\delta F}{\delta \eta_p(\vec{r},t)} + \varsigma_p(\vec{r},t) \qquad p = 1, \dots, n\,, \tag{1}$$

where L is the kinetic coefficient, $\frac{\delta F}{\delta \eta_p(\vec{r},t)}$ is the driving force for MT, and $\varsigma_p(\vec{r},t)$ is the Langevin noise characterizing the thermal fluctuation [53,74].

Chemical free energy and elastic strain energy are the components of the total free energy in the MT.

$$F = F_{ch} + F_{el}\,. \tag{2}$$

2.1.2.1. Chemical Free Energy

Following the Cahn and Hilliard's [75] approach for free energy definition for non-uniform systems, we can define the total chemical free energy for a medium containing both tetragonal and monoclinic phases as [53]:

$$F_{ch} = \int_V \left[f(\eta_1, \eta_2, \dots, \eta_n) + \frac{1}{2} \sum_{p=1}^{n} \beta_{ij}(p) \nabla_i \eta_p \nabla_j \eta_p \right] dV \qquad n = 1, \dots, p\,, \tag{3}$$

where $\beta_{ij}(p)$ is gradient energy coefficient tensor and $f(\eta_1, \eta_2 \dots, \eta_n)$ is the bulk chemical free energy and described as the following fourth-order Landau polynomial

$$f(\eta_1, \eta_2, \dots, \eta_n) = A(\sum_{p=1}^{n} \eta_p^2) + (4\Delta G - 2A)(\sum_{p=1}^{n} \eta_p^3) + (A - 3\Delta G)(\sum_{p=1}^{n} \eta_p^2)^2, \tag{4}$$

where A is a material property, and ΔG is the chemical driving force. A can be defined as $A_0(T - Tc), A_0 > 0$, where Tc is austenite, here tetragonal, critical temperature. The gradient energy coefficient is assumed to be isotropic ($\beta_{ij} = \beta \delta_{ij}$); So, we can simplify the chemical free energy:

$$F_{ch} = \int_V \left[f(\eta_1, \eta_2, \dots, \eta_n) + \frac{1}{2} \sum_{p=1}^{n} \beta (\nabla_i \eta_p)^2 \right] dV. \tag{5}$$

2.1.2.2. Elastic Strain Energy

The strain energy can be described following Khachaturyan [76] and using the transformation-induced stress free strain $\varepsilon_{ij}^0(\vec{r})$. Stress free strain quantifies the amount of lattice mismatch between the parent and product phases. The local stress free strain could be defined through [53]:

$$\varepsilon_{ij}^0(\vec{r}) = \sum_{p=1}^{n} \varepsilon_{ij}^{00}(p) \eta_p^2(\vec{r})\,, \tag{6}$$

where $\varepsilon_{ij}^{00}(p)$ is the transformation strain of p^{th} variant and can be calculated from the parent and product phases' crystallography and lattice parameters. Transformation strains of different monoclinic variants for $t \rightarrow m$ transformation in zirconia are listed in Table 1; we refer the interested readers to Ref. [70] for the detailed procedure on how these transformation strains are calculated. The following equation calculates the elastic strain energy of the system:

$$F_{el} = \frac{1}{2} \int_V \sigma_{ij} \varepsilon_{ij}^{el} dV = \frac{1}{2} \int_V C_{ijkl}^0 \varepsilon_{kl}^{el} \varepsilon_{ij}^{el} dV\,, \tag{7}$$

where the elastic strain, $\varepsilon_{ij}^{el}(\vec{r})$, is defined as

$$\varepsilon_{ij}^{el}(\vec{r}) = \varepsilon_{ij}^{tot}(\vec{r}) - \varepsilon_{ij}^0(\vec{r}). \tag{8}$$

So the total free energy for the MT is:

$$F = \int_V \left[f(\eta_1, \eta_2, \dots, \eta_n) + \frac{1}{2} \sum_{p=1}^{n} \beta \left(\Delta \eta_p \right)^2 \right] dV + \frac{1}{2} \int_V C_{ijkl}^0 \varepsilon_{ij}^{el} \varepsilon_{kl}^{el} dV\,. \tag{9}$$

Table 1. The transformation strain tensors for different monoclinic variants during tetragonal to monoclinic transformation in zirconia [70].

Variant			**Self-accommodating variant**		
Order parameter	Variant	Transformation strain (ε_{ij}^{00})	Order parameter	Variant	Transformation strain (ε_{ij}^{00})
η_1	ABC	$\begin{bmatrix} 0.0049 & 0 & -0.0760 \\ 0 & 0.0117 & 0 \\ -0.0760 & 0 & 0.0180 \end{bmatrix}$	η_2	$AB\overline{C}$	$\begin{bmatrix} 0.0049 & 0 & 0.0760 \\ 0 & 0.0117 & 0 \\ 0.0760 & 0 & 0.0180 \end{bmatrix}$
η_3	BAC	$\begin{bmatrix} 0.0117 & 0 & 0 \\ 0 & 0.0049 & -0.0760 \\ 0 & -0.0760 & 0.0180 \end{bmatrix}$	η_4	$BA\overline{C}$	$\begin{bmatrix} 0.0117 & 0 & 0 \\ 0 & 0.0049 & 0.0760 \\ 0 & 0.0760 & 0.0180 \end{bmatrix}$
η_5	ACB	$\begin{bmatrix} 0.0048 & -0.0769 & 0 \\ -0.0769 & 0.0418 & 0 \\ 0 & 0 & -0.0114 \end{bmatrix}$	η_6	$A\overline{C}B$	$\begin{bmatrix} 0.0048 & 0.0769 & 0 \\ 0.0769 & 0.0418 & 0 \\ 0 & 0 & -0.0114 \end{bmatrix}$
η_7	CAB	$\begin{bmatrix} 0.0418 & -0.0769 & 0 \\ -0.0769 & 0.0048 & 0 \\ 0 & 0 & -0.0114 \end{bmatrix}$	η_8	$\overline{C}AB$	$\begin{bmatrix} 0.0418 & 0.0769 & 0 \\ 0.0769 & 0.0048 & 0 \\ 0 & 0 & -0.0114 \end{bmatrix}$
η_9	BCA	$\begin{bmatrix} 0.0117 & 0 & 0 \\ 0 & 0.0419 & -0.0760 \\ 0 & -0.0760 & -0.0181 \end{bmatrix}$	η_{10}	$B\overline{C}A$	$\begin{bmatrix} 0.0117 & 0 & 0 \\ 0 & 0.0419 & 0.0760 \\ 0 & 0.0760 & -0.0181 \end{bmatrix}$
η_{11}	CBA	$\begin{bmatrix} 0.0419 & 0 & -0.0760 \\ 0 & 0.0117 & 0 \\ -0.0760 & 0 & -0.0181 \end{bmatrix}$	η_{12}	$\overline{C}BA$	$\begin{bmatrix} 0.0419 & 0 & 0.0760 \\ 0 & 0.0117 & 0 \\ 0.0760 & 0 & -0.0181 \end{bmatrix}$

For having a smooth transition in the elastic constants between the tetragonal and monoclinic phases, we use the following equation,

$$C_{ijkl}^{0} = C_{ijkl}^{T}\left[1 - \left(\sum_{p=1}^{n} \eta_p\right)\right] + C_{ijkl}^{M} \tag{10}$$

where C_{ijkl}^{T} and C_{ijkl}^{M} are tetragonal and monoclinic elastic constants.

The monoclinic elastic constant tensor has to be calculated for each monoclinic variant separately. The elastic constants of variant *ABC* are provided in Table 2, and we rotate the tensor properly to obtain different variants' elastic constants. We refer the interested readers to Mamivand et al. [70] for more details.

Table 2. The monoclinic zirconia elastic constants (Gpa).

C_{11}	C_{22}	C_{33}	C_{44}	C_{55}	C_{66}	C_{12}	C_{13}	C_{16}	C_{23}	C_{26}	C_{36}	C_{45}
361	408	258	100	81	126	142	55	-21	196	31	-18	-23

Table 3. The tetragonal zirconia elastic constants (Gpa).

C_{11}	C_{33}	C_{44}	C_{66}	C_{12}	C_{13}
327	264	59	64	100	62

2.2. Phase Field Modeling of Crack Growth

Francfort and Marigo [77] were the first who developed a variational framework for crack growth based on Griffith's theory [78]. In this formulation, the total potential energy, $\Psi_{pot}(u,\Gamma)$, is calculated by adding the elastic energy $\psi_\varepsilon(\varepsilon)$, fracture energy, and energy due to the external forces:

$$\Psi_{pot}(\vec{u},\Gamma) = \int_\Omega \psi_\varepsilon(\varepsilon_{ij})\, d\Omega + \int_\Gamma G_c\, dS - \int_\Omega \vec{b}.\vec{u}\, d\Omega - \int_{\partial\Omega_{h_i}} \vec{f}.\vec{u}\, dS\,, \tag{11}$$

where the linear strain tensor is described by,

$$\varepsilon_{ij} = \frac{1}{2}\left(\frac{\partial u_i}{\partial r_j} + \frac{\partial u_j}{\partial r_i}\right). \tag{12}$$

To describe the transition between the crack and uncracked domains, we need to define a PF variable $\phi(r,t) \in [0,1]$, with $\phi = 1$ indicates the crack, and $\phi = 0$ indicates the uncracked body, see Figure 3.

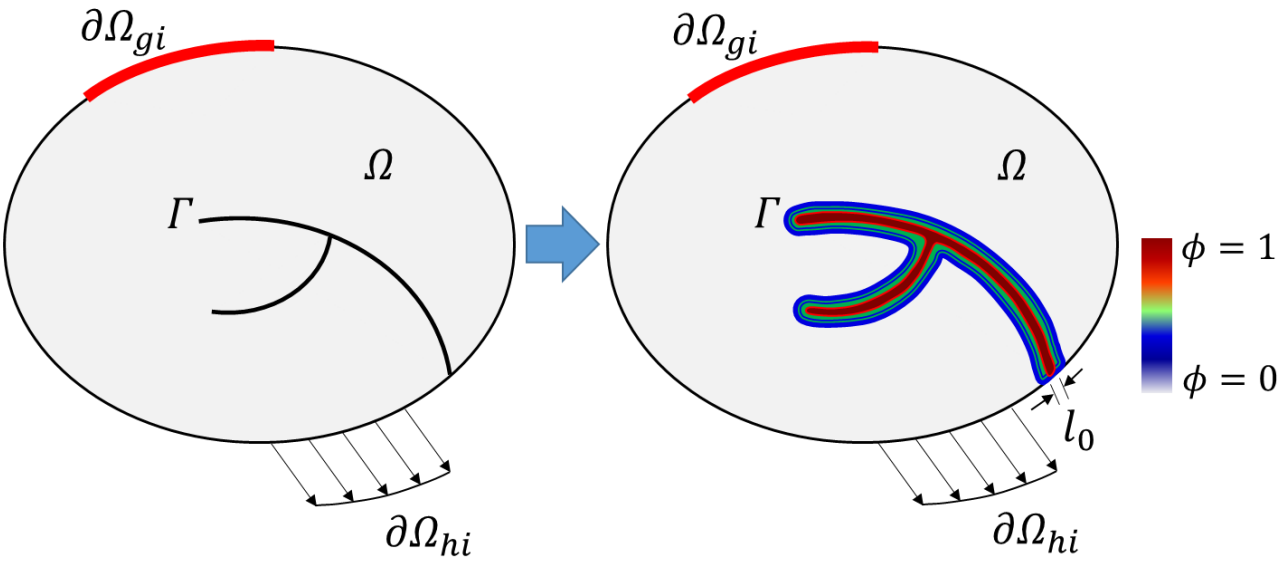

Figure 3. The crack surface approximation in phase field modeling for a smooth transition from crack to the uncracked domain.

The crack surface density per unit volume of the domain is defined as [65],

$$\gamma(\phi,\nabla\phi) = \left[\frac{\phi^2}{2l_0} + \frac{l_0}{2}\frac{\partial\phi}{\partial r_i}\frac{\partial\phi}{\partial r_i}\right] d\Omega\,, \tag{13}$$

where the length scale parameter l_0 regulates the transition zone between the crack and intact body.

From the crack surface density, the fracture energy can be calculated as,

$$\int_{\Gamma} G_c dS = \int_{\Omega} G_c \left[\frac{\phi^2}{2l_0} + \frac{l_0}{2}\frac{\partial\phi}{\partial r_i}\frac{\partial\phi}{\partial r_i}\right] d\Omega \,. \tag{14}$$

To prevent the crack growth under compression, which was an issue in the early PF models, the elastic strain is decomposed into spherical ε_{sph} and deviatoric ε_{dev} parts [79].

$$\psi_{\varepsilon}(\varepsilon_{ij},\phi) = \begin{cases} \frac{1}{2} g(\phi)\left[\varepsilon_{ij} C^0_{ijkl} \varepsilon_{kl}\right] & if\ tr(\varepsilon_{ij}) \geq 0 \\ \frac{1}{2}\left[\varepsilon^{sph}_{ij} C^0_{ijkl} \varepsilon^{sph}_{kl}\right] + g(\phi)\left[\varepsilon^{dev}_{ij} C^0_{ijkl} \varepsilon^{dev}_{kl}\right] & if\ tr(\varepsilon_{ij}) < 0 \end{cases}, \tag{15}$$

where C^0_{ijkl} is the elastic tensor given in Eq. (10) and the degradation function $g(\phi)$ is defined in the following form,

$$g(\phi) = (1-k)(1-\phi)^2 + k \,. \tag{16}$$

where k is a small number and helps in problem well-posedness.

Therefore, the elastic tensor can be described by,

$$C_{ijkl}(\phi) = g(\phi) C^0_{ijkl} + k_0 1 \otimes 1 [1 - g(\phi)] sign^{-}\left(tr(\varepsilon_{ij})\right). \tag{17}$$

Regarding the sign function if $x < 0$ then $sign^{-}(x) = 1$ and if $x \geq 0$ then $sign^{-}(x) = 0$. Therefore, it is now possible to reformat the strain energy density as,

$$\psi_{\varepsilon}(\varepsilon,\phi) = \frac{1}{2}\left[\varepsilon_{ij} C_{ijkl}(\phi) \varepsilon_{kl}\right]. \tag{18}$$

2.3. Coupling the Variational Formulation of Crack Growth to MT

The process of coupling the variational formalism of fracture with the PF framework of the MT is provided in the following.

The total free energy can be obtained by adding up the Eq. (9) and Eq. (11).

$$\begin{aligned} &\Psi_{pot}(\vec{u},\Gamma) = \int_{\Omega} \psi_{\varepsilon}(\varepsilon_{ij})\, d\Omega + \int_{\Gamma} G_c \, dS + \int_{\Omega} f(\eta_1,\eta_2,\dots,\eta_n) + \\ &\frac{1}{2}\sum_{p=1}^{n} \beta_{ij}(p) \nabla_i \eta_p \nabla_j \eta_p \, d\Omega - \int_{\Omega} \vec{b}.\vec{u}\, d\Omega - \int_{\partial\Omega \mathrm{h}_i} \vec{f}.\vec{u}\, dS \,. \end{aligned} \tag{19}$$

By substituting $f(\eta_1,\eta_2,\dots,\eta_n)$ from Eq. (4) and G_c from Eq. (14) and $\psi_{\varepsilon}(\varepsilon)$ from Eq. (18) we have:

$$\begin{aligned} &\Psi_{pot}(\vec{u},\Gamma) = \int_{\Omega} \frac{1}{2}\left[\varepsilon_{ij} C_{ijkl}(\phi) \varepsilon_{kl}\right] d\Omega + \int_{\Omega} G_c \left[\frac{\phi^2}{2l_0} + \frac{l_0}{2}\frac{\partial\phi}{\partial r_i}\frac{\partial\phi}{\partial r_i}\right] d\Omega + \int_{\Omega} [A(\sum_{p=1}^{n} \eta_p^2) + \\ &(4\Delta G - 2A)(\sum_{p=1}^{n} \eta_p^3) + (A - 3\Delta G)(\sum_{p=1}^{n} \eta_p^2)^2] d\Omega + \\ &\frac{1}{2}\sum_{p=1}^{n} \beta_{ij}(p) \nabla_i \eta_p \nabla_j \eta_p \, d\Omega - \int_{\Omega} \vec{b}.\vec{u}\, d\Omega - \int_{\partial\Omega \mathrm{h}_i} \vec{f}.\vec{u}\, dS \,. \end{aligned} \tag{20}$$

By minimizing the variation of the free energy functional, we can obtain the following governing equation:

$$2(1-k)(1-\phi)\left[\varepsilon_{ij}C^{h}_{ijkl}\varepsilon_{kl}\right]-2\Psi_c\left(\phi-{l_0}^2\nabla^2\phi\right)=0\,, \tag{21}$$

where $\Psi_c=\frac{G_c}{2l_0}$ and $C^{h}_{ijkl}=\frac{1}{2}\left(C^{0}_{ijkl}-k_0 1\otimes 1 sign^{-}\left(tr\left(\varepsilon_{ij}\right)\right)\right)$.

To consider loading and unloading histories, we follow the Miehe et al. [65] and define the strain history functional as:

$$\mathcal{H}(\vec{r},t)=\max_{\tau\in[0,t]}\left\{(1-k)\left[\varepsilon_{ij}C^{h}_{ijkl}\varepsilon_{kl}\right]\right\}. \tag{22}$$

By substituting Eq. (22) into the Eq. (21), we get:

$$(1-\phi)\mathcal{H}-\Psi_c\left(\phi-{l_0}^2\nabla^2\phi\right)=0\,. \tag{23}$$

Subsequently, after some mathematical operation, we have:

$$\left(1+\frac{\mathcal{H}}{\Psi_c}\right)\phi-{l_0}^2\nabla^2\phi=\frac{\mathcal{H}}{\Psi_c}\,. \tag{24}$$

Considering the coupled energy functional, the Ginzburg-Landau equation, Eq. (1), would have the following format:

$$\frac{\partial\eta_p(\vec{r},t)}{\partial t}=-L\left(-\beta\,\nabla^2\eta_p(\vec{r},t)+\frac{\partial f}{\partial\eta_p(\vec{r},t)}+\frac{\delta F_{el}}{\delta\eta_p(\vec{r},t)}\right)+\varsigma_p(\vec{r},t)\quad p=1,\dots,n \tag{25}$$

where f was described in Eq. (4), and

$$\begin{aligned}\frac{\delta F_{el}}{\delta\eta_p(\vec{r},t)}=&-\frac{1}{2}C_{ijkl}(\phi)\varepsilon^{00}_{kl}(p)\eta_p(\vec{r},t)\left(u_{i,j}(\vec{r})+u_{j,i}(\vec{r})\right)+\\&C_{ijkl}(\phi)\varepsilon^{00}_{kl}(p)\eta_p(\vec{r},t)\sum_{z=1}^{n}\varepsilon^{00}_{ij}(z)\eta^2_z(\vec{r},t)-\frac{1}{2}C_{ijkl}(\phi)\varepsilon^{00}_{ij}(p)\eta_p(\vec{r},t)\left(u_{k,l}(\vec{r})+\right.\\&\left.u_{l,k}(\vec{r})\right)+C_{ijkl}(\phi)\varepsilon^{00}_{ij}(p)\eta_p(\vec{r},t)\sum_{z=1}^{n}\varepsilon^{00}_{kl}(z)\eta^2_z(\vec{r},t)\end{aligned} \tag{26}$$

Regarding the mechanical equilibrium equations, we have:

$$\frac{\partial\sigma_{ij}}{\partial r_j}=0\Rightarrow C_{ijkl}(\phi)\left[\frac{1}{2}\left(u_{k,lj}(\vec{r})+u_{l,kj}(\vec{r})\right)-\sum_{p}\varepsilon^{00}_{kl}(p)\frac{\partial}{\partial r_j}\left(\eta^2_p(\vec{r})\right)\right]=0 \tag{27}$$

Finally, the governing equations for the crack propagation in the transformable domains would be Eqs. (24), (25), and (27) which are solved in a finite element package COMSOL with proper load and boundary conditions.

3. Results

In this section, we model the 3D single crystal zirconia fracture in a cube with a length of 2 μm. The cube has an initial crack and a monotonic increasing displacement load, $\Delta u = 1 \frac{nm}{s}$, has been applied at the upper surface, and the bottom boundary is clamped. A fine mesh has been applied. The geometry and boundary conditions are depicted in Figure 4.

The numerical parameters that are used in this model are provided in Table 4.

Table 4. Parameters applied in the model.

Temperature (K)	1170
A (N/m^2) [70]	2.5×10^6
Chemical driving force, $(J.mol^{-1})$ [70]	800 $(36.8 \times 10^6\ J.m^{-3})$
Gradient energy coefficient, $\beta\ (J.m^{-1})$ [70]	2.5×10^{-9}
Kinetic coefficient, $L\ (m^3.J^{-1}.s^{-1})$	2×10^{-9}
Critical energy release rate, $G_c(J.m^{-2})$ [29]	4.33
Crack elasticity modification parameter, k	1×10^{-9}
The length parameter, $l_0\ (nm)$	20

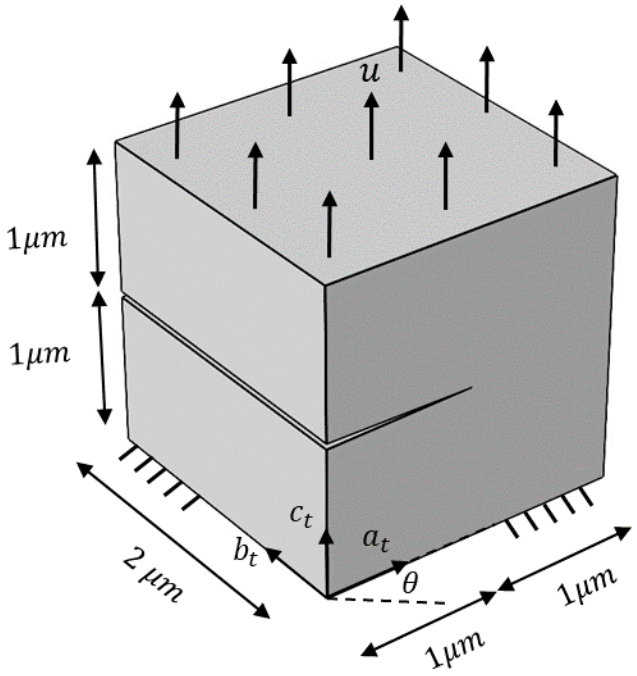

Figure 4. The boundary conditions and geometry of a cube with an initial crack.

3.1. Model Verification

We validate the proposed model by comparing the results with the experiments. Figure 5 shows a comparison between the PF model results and an Atomic Force Microscopy (AFM) micrograph of the surface relief obtained from the martensitic $t \rightarrow m$ transformation in ceria-stabilized zirconia [15]. The high resolution AFM experiments of Deville et al. [15] make it feasible to follow and capture the transition-induced relief at the surface precisely. AFM

observations at the crack zone in Figure 5 show self-accommodated martensite pairs development in the vicinity of crack areas with arrows indicating such pairs' junction planes. As in Deville et al. [15] experimental observations, transformed variants are distinctly visible when c_t axis of the grain is almost perpendicular to the surface. We adopt the same orientation for the single crystal in this simulation and the results depict similar morphologies for the monoclinic variants. Figure 5-a shows the crack pattern and the microstructure of the transformed domain from the simulation. Four different martensitic variants emerged from the simulation, namely ABC, $AB\bar{C}$, BAC and $BA\bar{C}$. Figure 5-b shows the surrounding of a propagated crack in ceria-stabilized zirconia, which depicts the martensitic variants in the transformed zone. A magnified frame of the crack zone, illustrated in Figure 5-c, shows the primary and secondary junction planes of the martensitic variants.

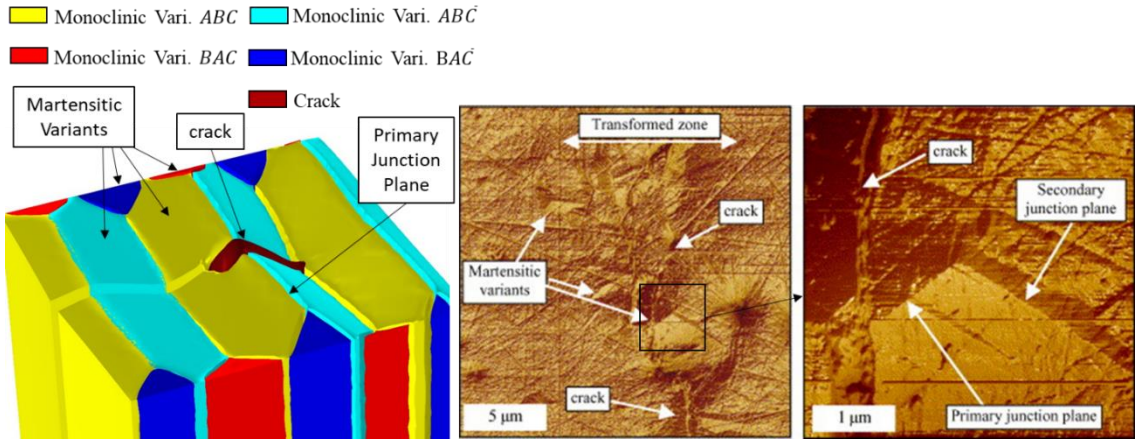

Figure 5. PF model simulation result for martensitic transformation and crack propagation in a 3D single crystal zirconia (a) and comparison with the experiment (b) (c) [15]. Figure (a) shows the crack pattern and the microstructure of the transformed domain from the simulation. Figure (b) shows Atomic Force Microscopy observations at the surrounding of a propagated crack in ceria-stabilized zirconia, which depicts the martensitic variants in the transformed zone. A magnified frame of the crack zone, illustrated in Figure (c), shows the primary and secondary junction planes of the martensitic variants.

The detailed investigation of Deville et al. [15] on transformation-induced relief leads to brand-new knowledge regarding the toughening mechanism order. Deville et al. [15] reported the fragmentation of the transformed zones caused by the crack growth. This observation indicates to the domain phase transition before the crack arrival. Phase field simulation also shows a similar observation, Figure 6. The reason behind this phenomenon is the fact that the stress state around the crack tip is increasing due to loading, and this stress can trigger the phase transformation, which absorbs some of the stress that otherwise would be available for crack growth. In the case of increasing the stress further, it leads to crack propagation in the transformed areas. Figure 6-c shows a propagated crack in ceria-stabilized zirconia. The crack propagated throughout the transformed grain and fragmented it. In this particular case, i.e. c_t is perpendicular to the top surface, we have a transformation strain that is accommodated vertically, so there is no residual stress in the domain, and it is possible for the crack to run through the transformed grain rather than passing alongside. Figure 6-a shows that the crack has started to grow while there are martensitic transformed variants in the domain, and the crack is passing through them. Figure 6-b shows that the crack propagated more and break the transformed plane.

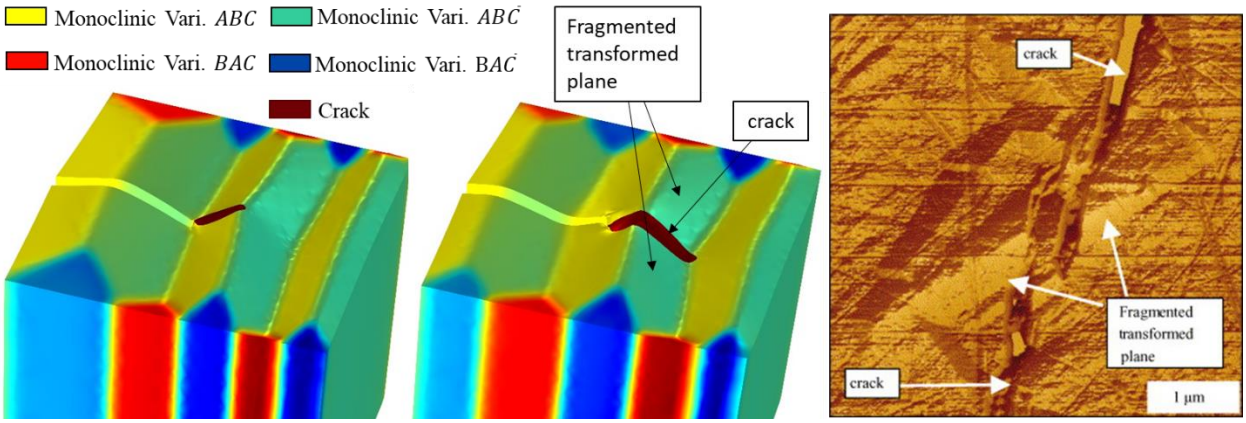

Figure 6. Observation of the fragmented transformed plane in both simulation (a)-(b) and experiment, AFM (c) [15]. Figure (a) shows that the crack has started to grow while there are martensitic transformed variants in the domain, and the crack is passing through them. Figure (b) shows that the crack propagated more and break the transformed plane. Figure (c) shows Atomic Force Microscopy observations of a propagated crack in zirconia showing that the crack propagated throughout the transformed grain and fragmented it.

3.2. Temporal and Spatial Evolution of Crack Propagation in Transformable Domains

In this section, we have considered the coupled PF model to investigate the crack growth, mode I, in a 3D tetragonal single crystal zirconia. In this part, we picked zero degrees, i.e., $\theta = 0°$, in Figure 4 for the lattice orientation angle. The results show the importance of the phase transformation on the crack growth as well as toughening.

Figure 7 depicts the co-evolution of $t \rightarrow m$ transformation and crack propagation in a 3D domain. The domain is fully tetragonal in the beginning. As the external loading is applied on the upper surface, the stress escalates at the crack tip and promotes the $t \rightarrow m$ transformation. As predicted from our simulation results and observed in the experimental studies, the phase transformation originates from the crack tip. The transition process proceeds by raising the displacement loading until the monoclinic phase dominants the crystal body.

Although there are 12 possible monoclinic variants in 3D, experimental studies have observed some of them more frequently. According to empirical and theoretical studies [80–82], correspondence *C* is the predominant direction for the transformation because of its relatively smaller strain energy than the other correspondences, i.e., *A* and *B*. The equations and model parameters are set in a way to consider all 12 monoclinic variants without any preferences or differences in their emergence chance and development. Nevertheless, only a few of them will show up in the final microstructure, which will be chosen by innate minimum formation energy principles.

For the current simulation set, i.e., the lattice orientation angle is zero degrees, $\theta = 0°$, only the monoclinic variants of ABC and $AB\bar{C}$ from the correspondence *C* show up in the microstructure, and the other variants do not appear while they have similar initial chances. After nucleation of favorable variants in the early stages of the phase transition, the variants rearrange and grow in a way to accommodate the highest possible amount of strain. When the monoclinic phase becomes dominant in the crystal, the crack propagates in its straight expected direction, as it is a mode I crack growth model. Since the model has the displacement loading normal to the upper boundary, which is the direction of c_t in this simulation, the correspondence *C* is expected to form and eventually change the microstructure until the whole upper crack part alters to the single monoclinic variant. This phenomenon agrees with the experimental and theoretical studies that observed the development of different martensitic variants in favor of the loading conditions [32,83].

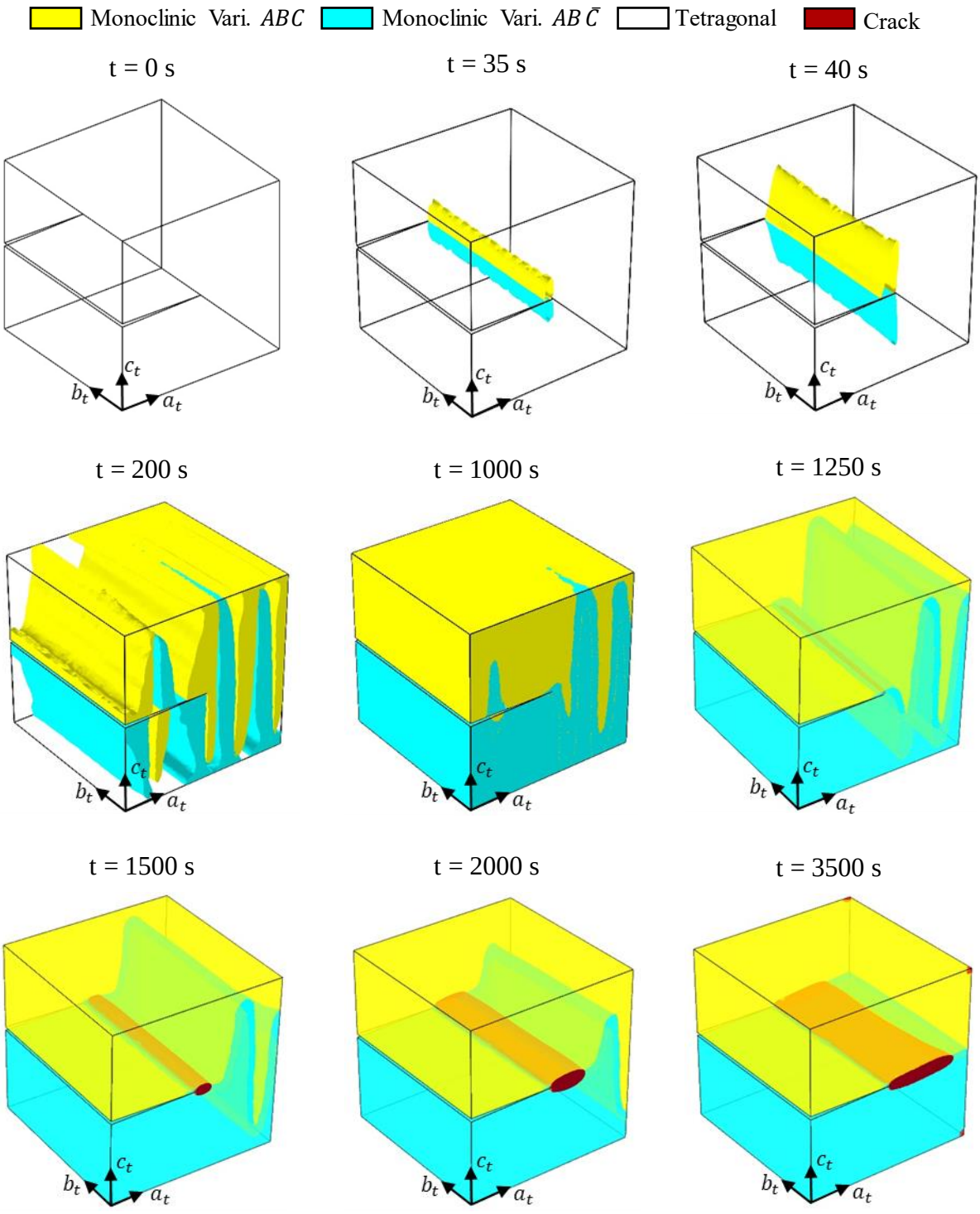

Figure 7. The concurrent evolution of $t \rightarrow m$ transformation and monoclinic variants reorientation with crack propagation in 3D single crystal zirconia in isosurface ($\eta = 0.5$). (Vacant domain is tetragonal, yellow is monoclinic variant ABC, cyan is monoclinic variant $AB\bar{C}$, and brown is crack)

To demonstrate the process of transformation toughening we have compared, in Figure 8, the stress-strain curves for the edge notched 3D single crystal for transformable and untransformable zirconia. Figure 8 shows that the fracture happens at the higher stresses for the transformable zirconia compared to the untransformable one, which indicates to the transformation toughening effect. We also note that the crack grows much further in untransformable zirconia due to the lack of transformation toughening effects. The difference between the stress-strain curves in Figure 8 at the early stages of loading is due to the t→m transformation which leads to a flat stress-strain curve for the transformable case.

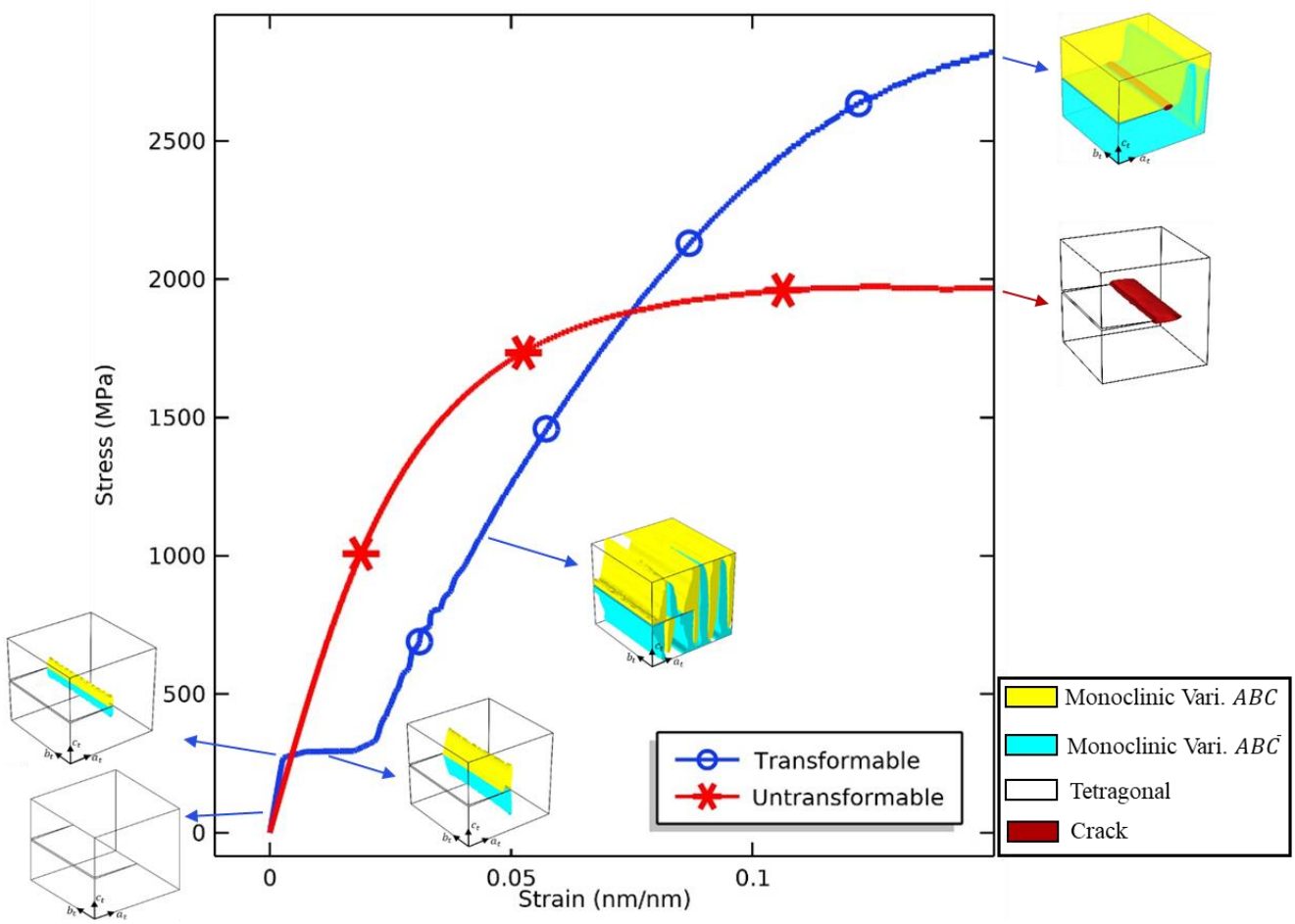

Figure 8. The stress-strain curve for transformable and untransformable 3D single crystal tetragonal zirconia.

3.1. The Effects of Crystal Lattice Orientation

To gain more profound knowledge on how the lattice orientation would affect the monoclinic variants formation and crack growth pattern and toughening, we have studied a set of simulations for crack growth in a 3D single crystal zirconia for different lattice orientations (LORs) in the a_t-c_t plane, i.e., the rotation angle is around the b_t-axis.

Figure 9 depicts the microstructure at t = 200 s and 2000 s and the crack pattern at t = 2000 s for the lattice orientations of 0, 15, 30, 45, 60, 75, and 90 degrees. The results show that the initial emerging and final monoclinic variants are different for different lattice orientations. For instance, in the models with LOR 0° and 15°, only monoclinic variants of ABC and $AB\bar{C}$ form. However, the arrangement of these variants are different in LOR 0° and 15°; the dominant twin plane for LOR 0° is $(100)_m$ plane, while for LOR 15°, we see both $(100)_m$ and $(001)_m$ planes. For LOR 0°, the crack grows evenly through the thickness while it is not even for LOR 15°. For 30°, 45°, and 60° we observe the formation of four monoclinic variants, i.e., ABC, $AB\bar{C}$, BAC and $BA\bar{C}$. The presence of ABC and $AB\bar{C}$ variants are more dominant for LOR 30° while the dominancy changes to BAC and $BA\bar{C}$ variants for LOR 60°. For LOR 75° and 90° only variants BAC and $BA\bar{C}$ form. The results reveal the profound influence of the lattice orientation on both

microstructure and crack growth. As the lattice orientation changes, the configuration and the type of the monoclinic variants alter, affecting the crack pattern and crack propagation amount or toughness. For instance, in the model with LOR 0°, the crack grows in a straight path and even throughout the thickness, because the displacement loading is in the c_t direction and the ABC and $AB\bar{C}$ monoclinic variants emerge symmetrically, whereas, in the model with LOR 15°, the crack is not even within the thickness because of the uneven microstructure formation that leads to the different stress states at various spots. Regarding the emerged microstructures, we note that in all simulations only the variants of the correspondence *C*, i.e. ABC, $AB\bar{C}$, BAC, and $BA\bar{C}$, form. It is primarily because the volumetric strain associate with these variants, i.e. 0.0346, is smaller than the volumetric strain associate with the variants of correspondence *A*, i.e. 0.0355, and correspondence *B*, i.e. 0.0352, see Table 1.

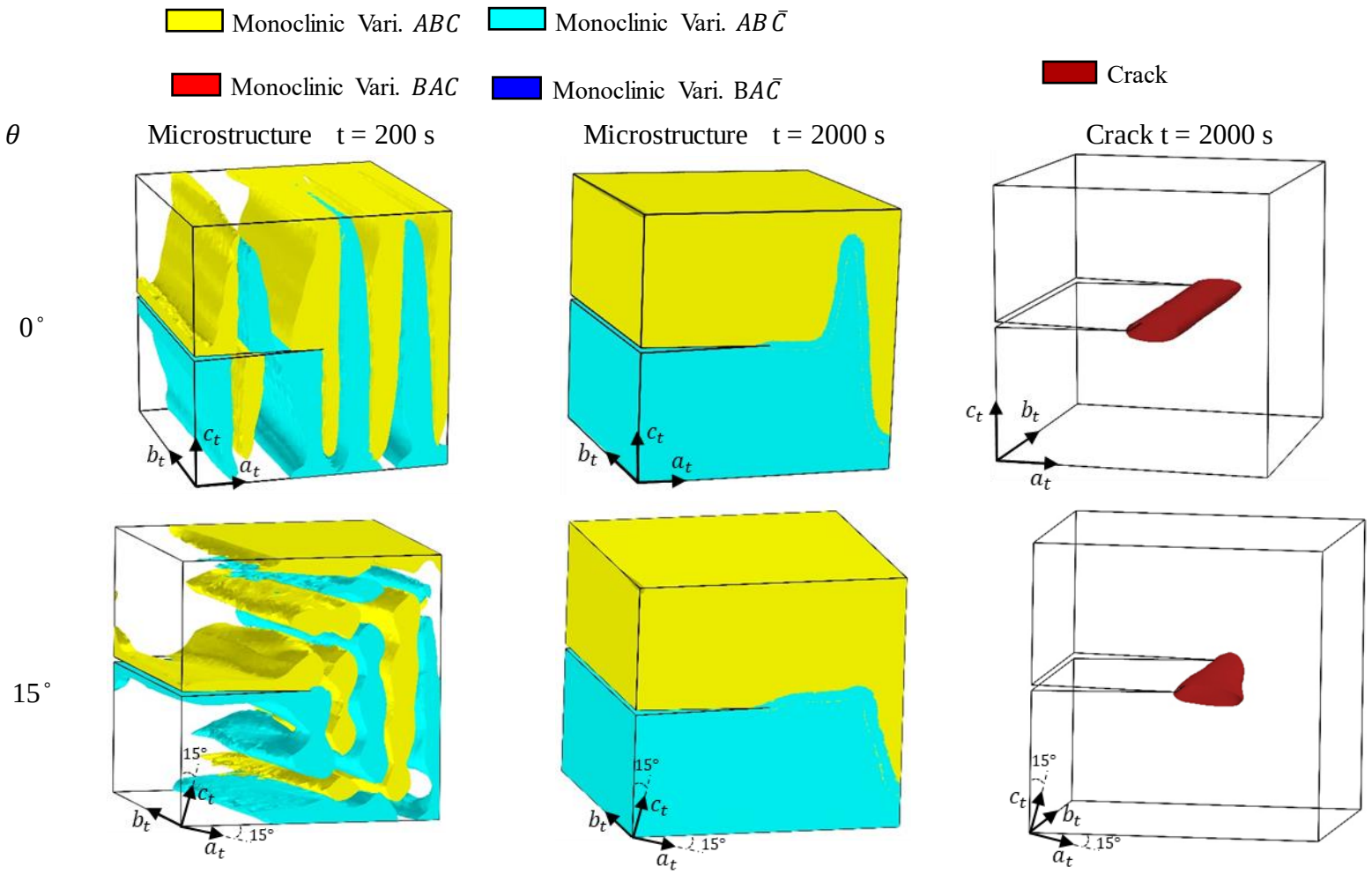

30˚

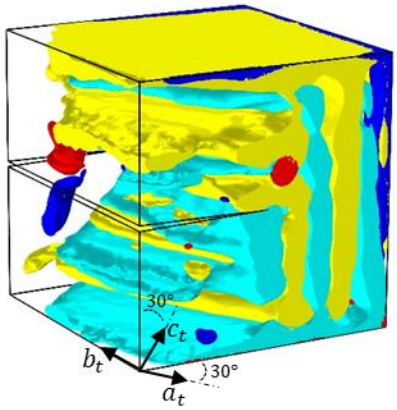

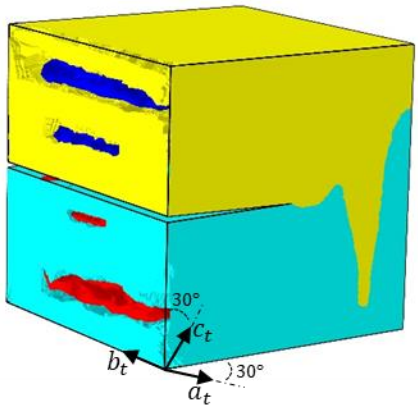

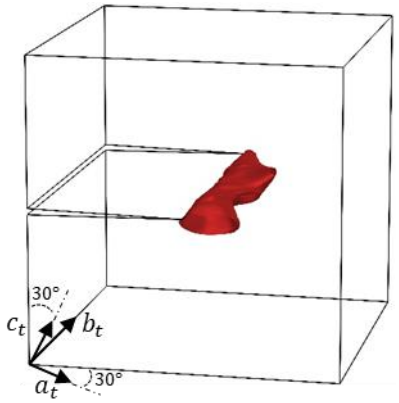

45˚

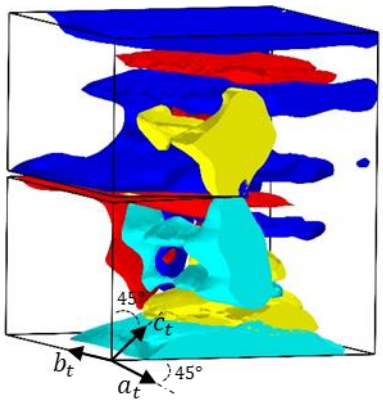

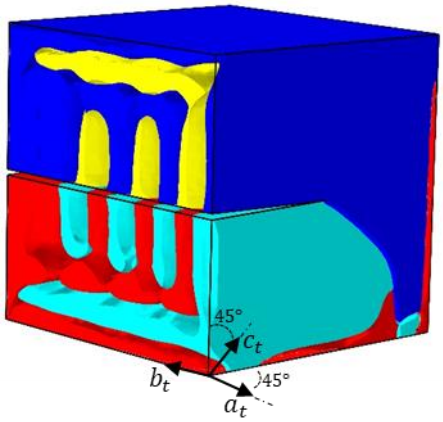

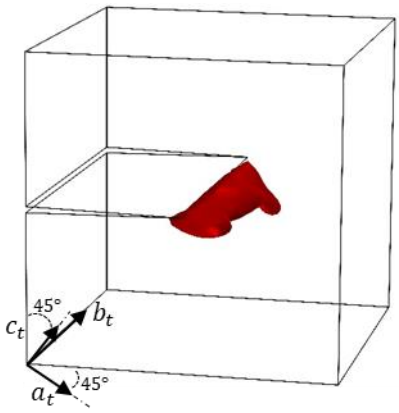

60˚

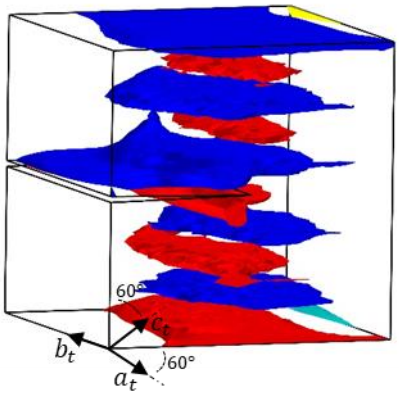

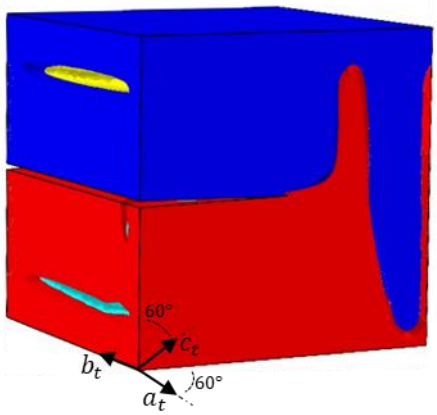

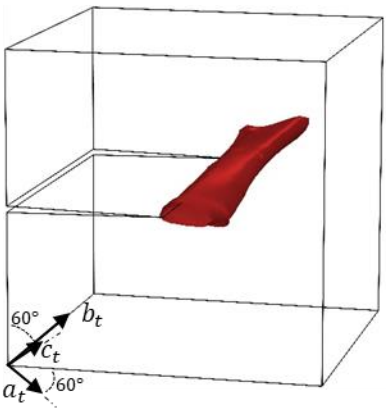

75˚

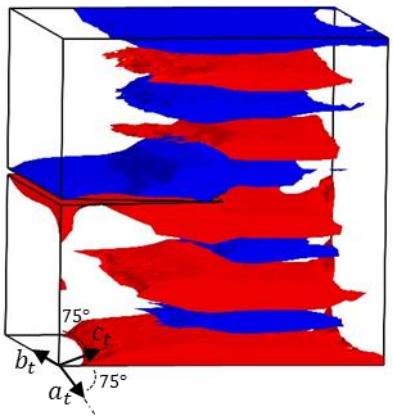

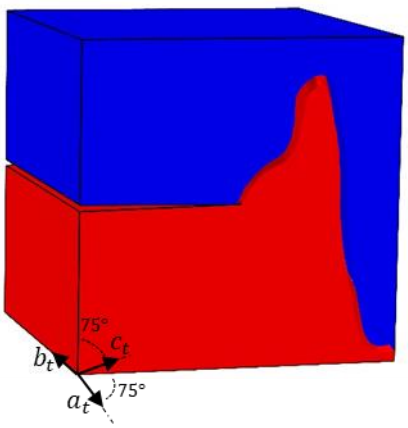

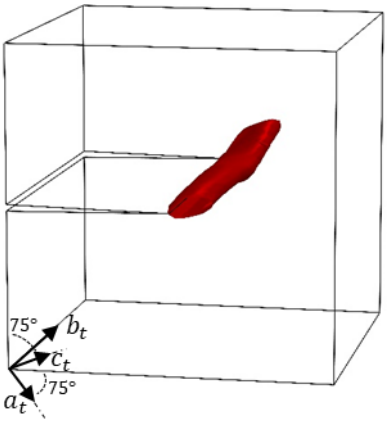

90˚

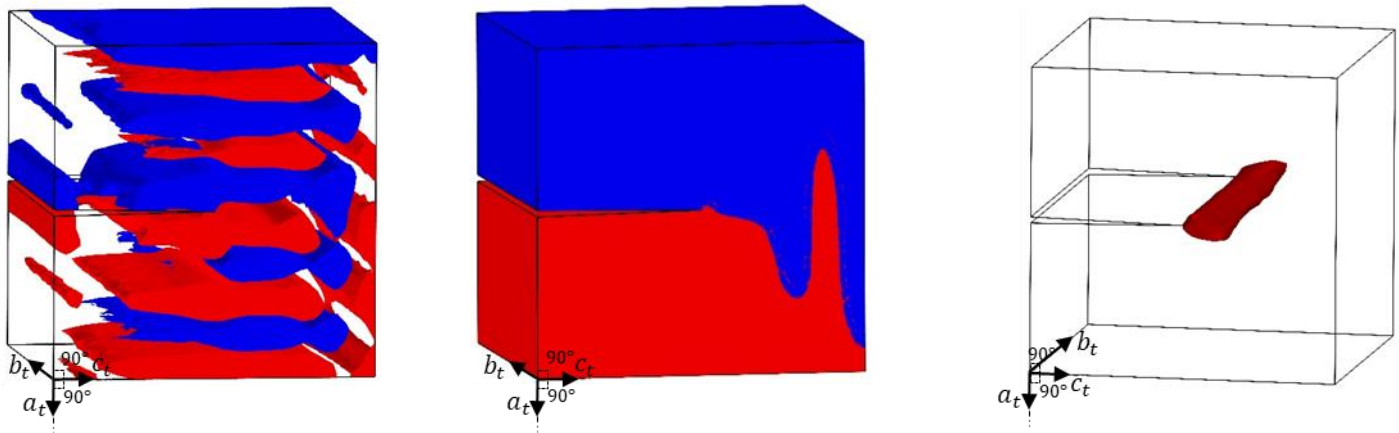

Figure 9. Microstructure and crack pattern in 3D single crystal zirconia with different lattice orientations. The first column shows the microstructure at t = 200 s, the second column shows the microstructure at t = 2000 s, and the last column shows the crack pattern at t = 2000 s.

To elaborate the concurrent evolution of crack and $t \rightarrow m$ transformation for the cases that the crack propagation deviates from the even growth through the thickness and gets deflected from the initial crack plane, we present the temporal and spatial concurrent evolution of MT and crack for LOR 30º in Figure 10. Originally, the entire crystal body is tetragonal. In the early stages of the loading, among all 12 possible variants of monoclinic, only four monoclinic variants, i.e., ABC, $AB\bar{C}$, BAC and $BA\bar{C}$, form at the crack tip because of the high stress concentration. The monoclinic variants rearrange to accommodate the maximum strain. The crack starts to grow when most of the crystal body has converted to monoclinic.

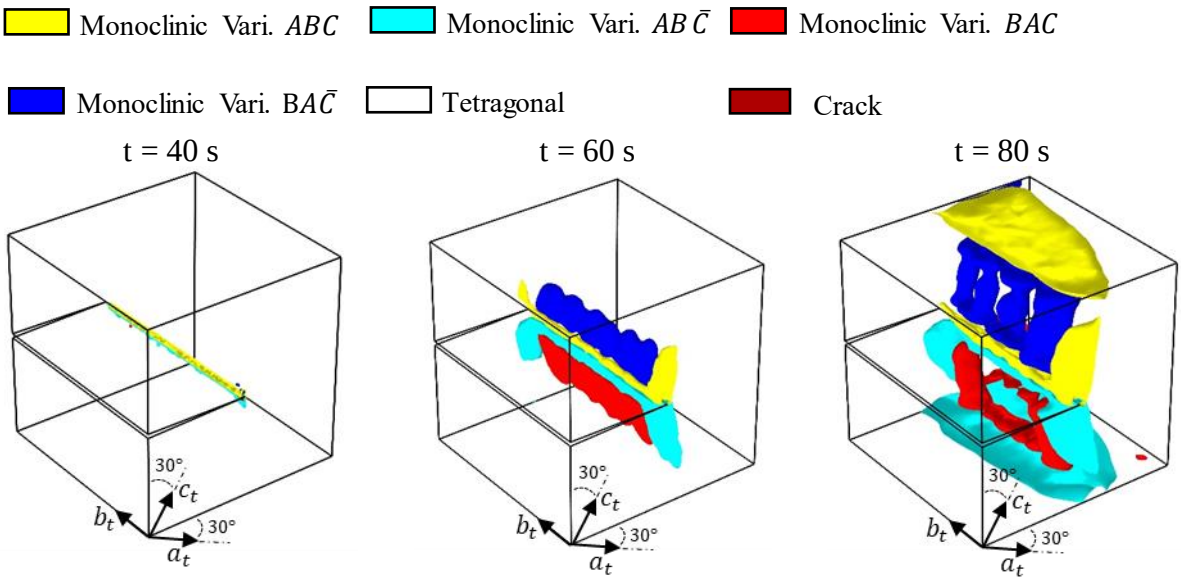

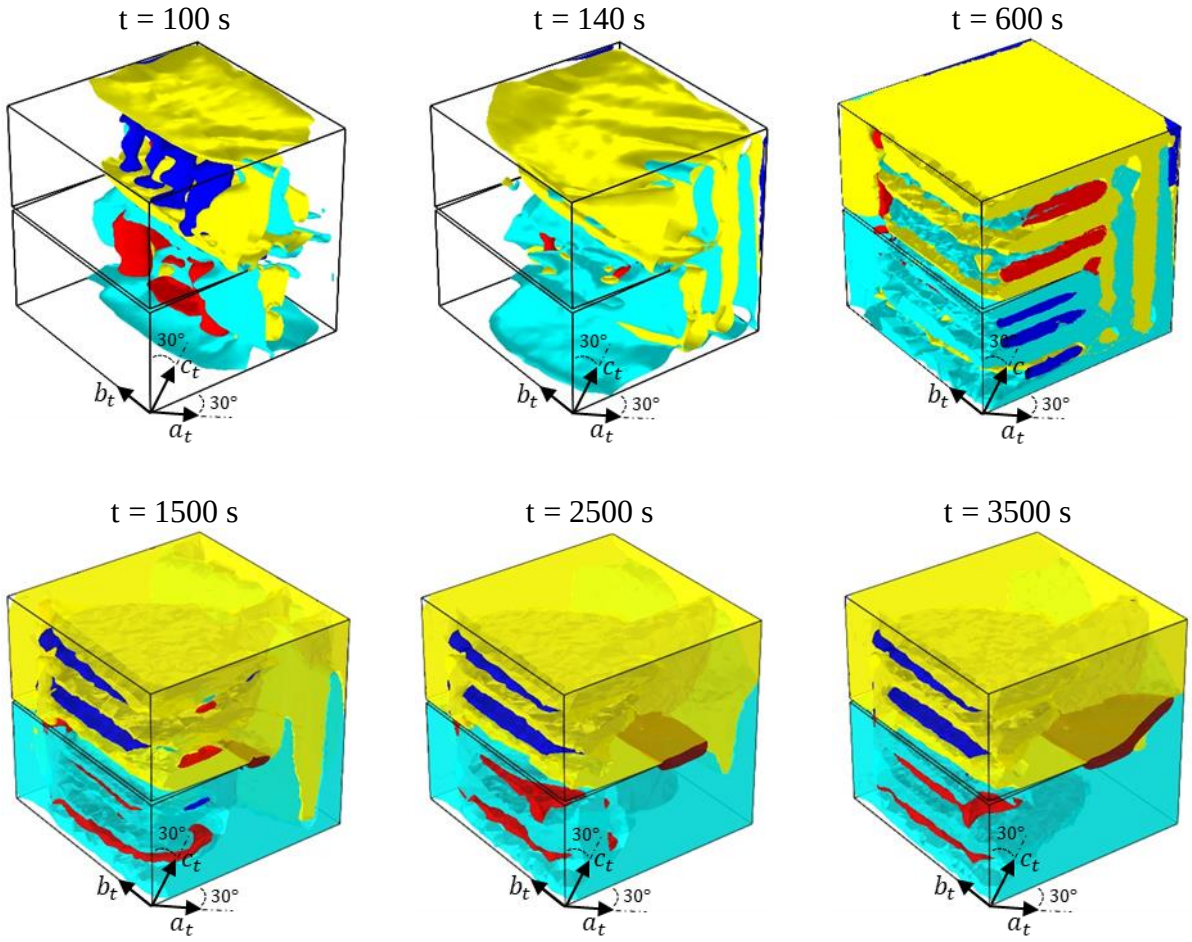

Figure 10. The temporal and spatial co-evolution of MT and crack for lattice orientation of 30 degrees in 3D single crystal zirconia.

To show the crack pattern clearly, we have removed the microstructure in Figure 11. Figure 11 (a)-(b) show that the crack starts growing at the t = 1100 s at $(0\bar{1}0)_t$ plane and then gradually propagates through the thickness. The difference in the crack growth amount is because of the phase transformation's local toughening effects, which vary at different locations, and consequently, these local monoclinic variants determine the stress states and crack growth driving force. This observation shows the impact of the local microstructure on the transformation toughening in shape memory ceramics. When monoclinic variants arrangement is in a way that produces more toughening, it is difficult for the crack to grow in some spots and vice versa. Figure 11(d) shows the crack pattern at t = 3500 s. At this stage, the crack has deflected upward in the $(0\bar{1}0)_t$ plane, while it is deflected slightly downward in the $(010)_t$ plane. Interestingly the uneven crack tip pattern through the thickness is not uniform; it is parabolic initially and then gets linear, Figure 11(e). This behavior is because of the evolving microstructural patterns constructed from different monoclinic variants in each spot; they create different local stresses through the thickness. Therefore, the crack tip pattern is not uniform and grows more in areas with more favorable stress states. Looking more closely at the microstructures, it turns out that the crack tip at $(0\bar{1}0)_t$ plane is more surrounded by monoclinic variant ABC and have the monoclinic variant $AB\bar{C}$ at the bottom. The configuration of monoclinic variants and the accommodated stress state in $(0\bar{1}0)_t$ plane leads to the upward deflection of the crack, whereas crack tip in the $(010)_t$ plane is surrounded almost evenly by variants ABC and $AB\bar{C}$ which leads to slight downward deflection. The presence of monoclinic variants $BA\bar{C}$ in the $(010)_t$ plane is the reason that the crack in this plane started very late compare to the other areas. Additionally, the middle part of the crack is surrounded by monoclinic variants $\bar{C}$, which made it difficult for this part of the crack to grow at the same pace as the other sections and eventually leading to the parabolic pattern of the crack tip in this area.

Since in this simulation we have lattice orientation of 30 degrees, the loading direction is not aligned with the c_t-axis and this leads to an unbalanced and un-symmetrical microstructural domain. This would result in uneven stress state at crack tip in different areas, resulting in an uneven crack growth throughout the thickness. The non-uniform growth of the crack tip through the thickness, which the 3D simulation enables us to observe, indicates to the local behavior of transformation toughening within a single crystal zirconia.

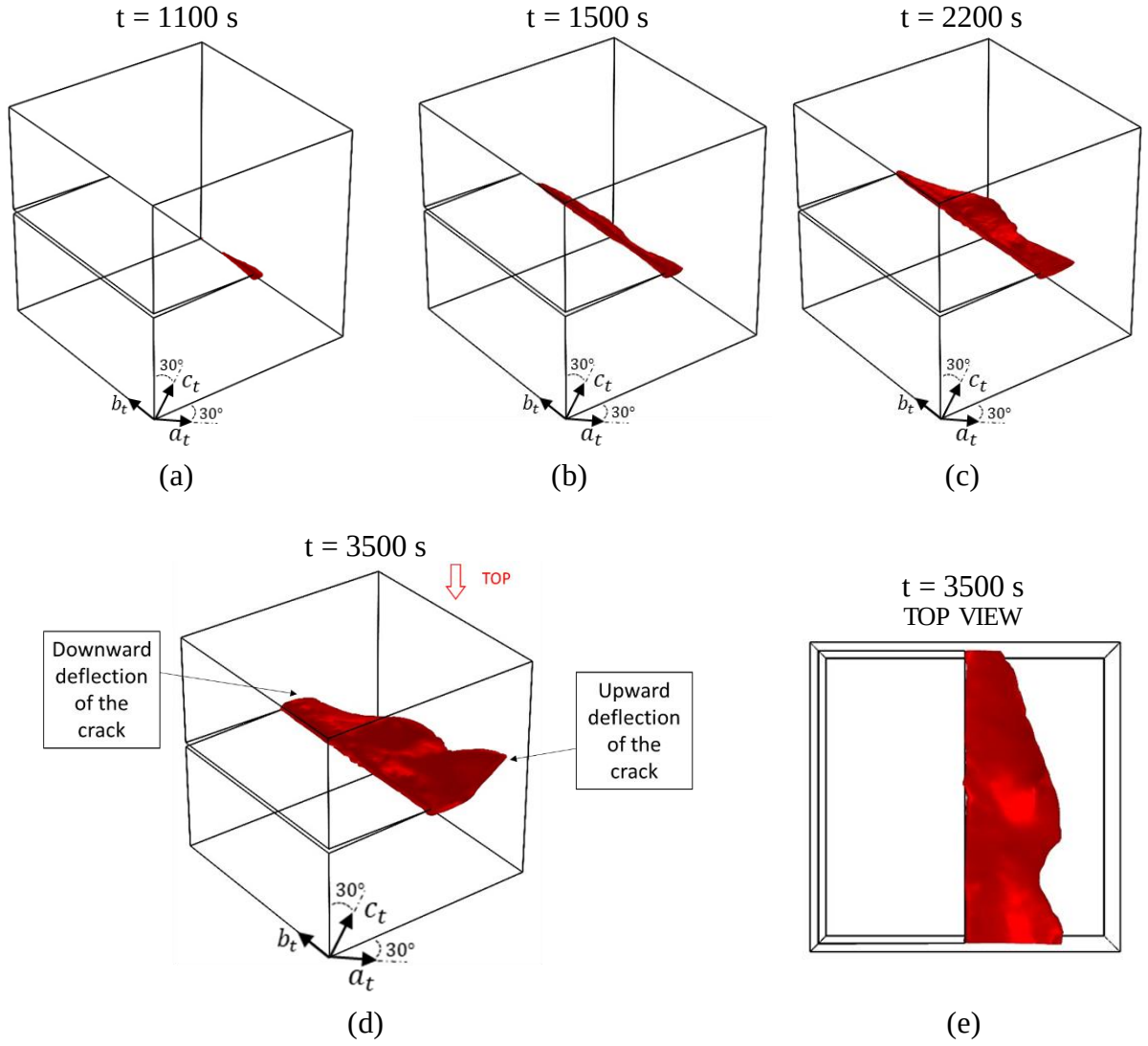

Figure 11. The Isosurface plots of the crack propagation in a single crystal zirconia for lattice orientation of 30 degrees around b_t-axis.

4. Conclusion

This work presented a three-dimensional phase field model to study the concurrent evolution of martensitic transformation and crack growth in the shape memory ceramics. Zirconia is used as the model material with emphasis on the tetragonal to monoclinic transformation. The three-dimensional modeling empowers us to acquire all the twelve variants of the monoclinic phase. By implementing all twelve monoclinic variants in the martensitic transformation model's equations and coupling them with the variational formulation of fracture, the developed model predicts the experimentally observed results, such as the surface uplifting and self-accommodated martensite formation in the crack vicinity. The model also agrees with the experimentally observed fragmented transformed zones resulting from the crack propagation throughout the transformed planes. Investigating the lattice orientation effects on zirconia fracture reveals the "local" nature of transformation toughening within a single crystal. Results also show that the

angles that the tetragonal axes make with the loading direction profoundly impact the selection of the monoclinic variants that nucleate at the crack tip and their further growth and eventual morphology and consequently on the crack growth path and toughening.

Data Availability: The raw/processed data required to reproduce these findings cannot be shared at this time as the data also forms part of an ongoing study.

Acknowledgments: The authors appreciate the support of Boise State University.

References

[1] Chevalier J, Gremillard L, Virkar A V., Clarke DR. The Tetragonal-Monoclinic Transformation in Zirconia: Lessons Learned and Future Trends. J Am Ceram Soc 2009;92:1901–20. https://doi.org/10.1111/j.1551-2916.2009.03278.x.

[2] GARVIE RC, HANNINK RH, PASCOE RT. Ceramic steel? Nature 1975;258:703–4. https://doi.org/10.1038/258703a0.

[3] Hannink RH, Kelly PM an. M, C B. Transformation toughening in zirconia-containing ceramics,. J Am Ceram Soc 2000;83:461–87.

[4] Lai A, Du Z, Gan CL, Schuh CA. Shape Memory and Superelastic Ceramics at Small Scales. Science (80-) 2013;341:1505. https://doi.org/10.1126/science.1239745.

[5] CLARKE DR, ADAR F. Measurement of the Crystallographically Transformed Zone Produced by Fracture in Ceramics Containing Tetragonal Zirconia. J Am Ceram Soc 1982;65:284–8. https://doi.org/https://doi.org/10.1111/j.1151-2916.1982.tb10445.x.

[6] Michel D, Mazerolles L, Perez Y Jorba M. Fracture of metastable tetragonal zirconia crystals. J Mater Sci 1983;18:2618–28. https://doi.org/10.1007/BF00547578.

[7] Hannnink RHJ, Swain M V. Metastability of the Martensitic Transformation in a 12 mol% Ceria-Zirconia Alloy: I, Deformation and Fracture Observations. J Am Ceram Soc 1989;72:90–8. https://doi.org/https://doi.org/10.1111/j.1151-2916.1989.tb05959.x.

[8] Loganathan A, Gandhi AS. Effect of phase transformations on the fracture toughness of t′ yttria stabilized zirconia. Mater Sci Eng A 2012;556:927–35. https://doi.org/https://doi.org/10.1016/j.msea.2012.07.095.

[9] Benzaid R, Chevalier J, Saâdaoui M, Fantozzi G, Nawa M, Diaz LA, et al. Fracture toughness, strength and slow crack growth in a ceria stabilized zirconia–alumina nanocomposite for medical applications. Biomaterials 2008;29:3636–41. https://doi.org/https://doi.org/10.1016/j.biomaterials.2008.05.021.

[10] Deville S, Chevalier J, El Attaoui H. Atomic Force Microscopy Study and Qualitative Analysis of Martensite Relief in Zirconia. J Am Ceram Soc 2005;88:1261–7. https://doi.org/10.1111/j.1551-2916.2005.00174.x.

[11] Kobayashi K, Kuwajima H, Masaki T. Phase change and mechanical properties of ZrO2-Y2O3 solid electrolyte after ageing. Solid State Ionics 1981;3–4:489–93. https://doi.org/https://doi.org/10.1016/0167-2738(81)90138-7.

[12] Evans AG. Toughening mechanisms in Zirconia Alloys. United States: American Ceramic Society, Inc; 1983.

[13] Hayakawa M, Oka M. Structural study on the tetragonal to monoclinic transformation in arc-melted ZrO2-2mol.%Y2O3—II. Quantitative analysis. Acta Metall 1989;37:2229–35. https://doi.org/https://doi.org/10.1016/0001-6160(89)90149-1.

[14] Wang XL, Fernandez-Baca JA, Hubbard CR, Alexander KB, Becher PF. Transformation behavior in Al2O3single bondZrO2 ceramic composites. Phys B Condens Matter 1995;213–214:824–6. https://doi.org/10.1016/0921-4526(95)00292-H.

[15] Deville S, El Attaoui H, Chevalier J. Atomic force microscopy of transformation toughening in ceria-stabilized zirconia. J Eur Ceram Soc 2005;25:3089–96. https://doi.org/https://doi.org/10.1016/j.jeurceramsoc.2004.07.029.

[16] McMEEKING RM, EVANS AG. Mechanics of Transformation-Toughening in Brittle Materials. J Am Ceram Soc 1982;65:242–6. https://doi.org/10.1111/j.1151-2916.1982.tb10426.x.

[17] Budiansky B, Hutchinson JW, Lambropoulos JC. Continuum theory of dilatant transformation toughening in ceramics. Int J Solids Struct 1983;19:337–55. https://doi.org/10.1016/0020-7683(83)90031-8.

[18] LAMBROPOULOS JC. Effect of Nucleation on Transformation Toughening. J Am Ceram Soc 1986;69:218–22. https://doi.org/10.1111/j.1151-2916.1986.tb07411.x.

[19] Stump DM, Budiansky B. Crack-growth resistance in transformation-toughened ceramics. Int J Solids Struct 1989;25:635–46. https://doi.org/10.1016/0020-7683(89)90030-9.
[20] Chen I-W. Model of Transformation Toughening in Brittle Materials. J Am Ceram Soc 1991;74:2564–72. https://doi.org/10.1111/j.1151-2916.1991.tb06800.x.
[21] Stam GTM, van der Giessen E, Meijers P. Effect of transformation-induced shear strains on crack growth in zirconia-containing ceramics. Int J Solids Struct 1994;31:1923–48. https://doi.org/10.1016/0020-7683(94)90200-3.
[22] Evans AG, Cannon RM. Toughening of brittle solids by martensitic transformations. Acta Metall 1986;34:761–800.
[23] Kelly PM, Francis Rose LR. The martensitic transformation in ceramics — its role in transformation toughening. Prog Mater Sci 2002;47:463–557. https://doi.org/10.1016/S0079-6425(00)00005-0.
[24] Celli A, Tucci A, Esposito L, Palmonari C. Fractal analysis of cracks in alumina–zirconia composites. J Eur Ceram Soc 2003;23:469–79. https://doi.org/10.1016/S0955-2219(02)00148-6.
[25] Freed Y an. B-S, L. Crack growth resistance of shape memory alloys by means of a cohesive zone model,. J Mech Phys Solids 2007;55:2157–80.
[26] Baxevanis T, Parrinello AF an. L, C D. On the fracture toughness enhancement due to stress-induced phase transformation in shape memory alloys,. Int J Plast 2013;50:158–69.
[27] Baxevanis T, Parrinello AF an. L, C D. On the driving force for crack growth during thermal actuation of shape memory alloys,. J Mech Phys Solids 2016;89:255–71.
[28] Baxevanis T, Landis C, Lagoudas D. On the Fracture Toughness of Pseudoelastic Shape Memory Alloys. J Appl Mech 2014;81. https://doi.org/10.1115/1.4025139.
[29] Zhao T, Zhu J, Luo J. Study of crack propagation behavior in single crystalline tetragonal zirconia with the phase field method. Eng Fract Mech 2016;159:155–73. https://doi.org/10.1016/J.ENGFRACMECH.2016.03.035.
[30] Zhu J, Luo J. Study of transformation induced intergranular microcracking in tetragonal zirconia polycrystals with the phase field method. Mater Sci Eng A 2017;701:69–84. https://doi.org/10.1016/j.msea.2017.06.060.
[31] Mamivand M, Asle Zaeem M, El Kadiri H, Chen L-Q. Phase field modeling of the tetragonal-to-monoclinic phase transformation in zirconia. Acta Mater 2013;61:5223–35. https://doi.org/10.1016/j.actamat.2013.05.015.
[32] Mamivand M, Asle Zaeem M, El Kadiri H. Phase field modeling of stress-induced tetragonal-to-monoclinic transformation in zirconia and its effect on transformation toughening. Acta Mater 2014;64:208–19. https://doi.org/10.1016/j.actamat.2013.10.031.
[33] Mamivand M, Asle Zaeem M, El Kadiri H. Shape memory effect and pseudoelasticity behavior in tetragonal zirconia polycrystals: A phase field study. Int J Plast 2014;60:71–86. https://doi.org/10.1016/j.ijplas.2014.03.018.
[34] S. Aranson I, Kalatsky VA, Vinokur V. Continuum Field Description of Crack Propagation. vol. 85. 2000. https://doi.org/10.1103/PhysRevLett.85.118.
[35] Karma A, Kessler DA, Levine H. Phase-Field Model of Mode III Dynamic Fracture. Phys Rev Lett 2001;87:45501. https://doi.org/10.1103/PhysRevLett.87.045501.
[36] Hakim V, Karma A. Laws of crack motion and phase-field models of fracture. J Mech Phys Solids 2009;57:342–68. https://doi.org/10.1016/j.jmps.2008.10.012.
[37] Spatschek R, Brener E, Karma A. Phase field modeling of crack propagation. Philos Mag 2011;91:75–95. https://doi.org/10.1080/14786431003773015.
[38] Eastgate LO, Sethna JP, Rauscher M, Cretegny T, Chen C-S, Myers CR. Fracture in mode I using a conserved phase-field model. Phys Rev E 2002;65:36117. https://doi.org/10.1103/PhysRevE.65.036117.
[39] Henry H, Levine H. Dynamic Instabilities of Fracture under Biaxial Strain Using a Phase Field Model. Phys Rev Lett 2004;93:105504. https://doi.org/10.1103/PhysRevLett.93.105504.
[40] Kumar A, Sørensen B. Fracture Resistance and Stable Crack-Growth Behavior of 8-mol%-Yttria-Stabilized Zirconia. J Am Ceram Soc 2004;83:1199–206. https://doi.org/10.1111/j.1151-2916.2000.tb01354.x.
[41] Moshkelgosha E, Mamivand M. Anisotropic Phase-Field Modeling of Crack Growth in Shape Memory Ceramics: Application to Zirconia. Vol 12 Adv Mater Des Process Charact Appl 2019;12:9. https://doi.org/10.1115/IMECE2019-11695.
[42] Moshkelgosha E, Mamivand M. Phase field modeling of crack propagation in shape memory ceramics – Application to zirconia. Comput Mater Sci 2020;174:109509. https://doi.org/10.1016/J.COMMATSCI.2019.109509.

[43] Moshkelgosha E, Mamivand M. Concurrent modeling of martensitic transformation and crack growth in polycrystalline shape memory ceramics. Eng Fract Mech 2020:107403. https://doi.org/10.1016/j.engfracmech.2020.107403.
[44] Jin YM, Wang YU, Khachaturyan AG. Three-dimensional phase field microelasticity theory and modeling of multiple cracks and voids. Appl Phys Lett 2001;79:3071–3. https://doi.org/10.1063/1.1418260.
[45] Loginova I, Odqvist J, Amberg G, Aagren J. The phase-field approach and solute drag modeling of the transition to massive $\gamma \rightarrow \alpha$ transformation in binary Fe-C alloys. Acta Mater 2003;51:1327–39. https://doi.org/10.1016/S1359-6454.
[46] Moelans N, Blanpain B, Wollants P. An introduction to phase-field modeling of microstructure evolution. Calphad 2008;32:268–94. https://doi.org/10.1016/j.calphad.2007.11.003.
[47] Boettinger WJ, Warren JA, Beckermann C, Karma A. Phase-Field Simulation of Solidification. Annu Rev Mater Res 2002;32:163–94. https://doi.org/10.1146/annurev.matsci.32.101901.155803.
[48] Zaeem MA, Yin H, Felicelli SD. Comparison of Cellular Automaton and Phase Field Models to Simulate Dendrite Growth in Hexagonal Crystals. J Mater Sci Technol 2012;28:137–46. https://doi.org/10.1016/S1005-0302(12)60034-6.
[49] Chen L-Q. Phase-Field Models for Microstructure Evolution. Annu Rev Mater Res 2002;32:113–40. https://doi.org/10.1146/annurev.matsci.32.112001.132041.
[50] Zaeem MA, Mesarovic SD. Finite element method for conserved phase fields: Stress-mediated diffusional phase transformation. J Comput Phys 2010;229:9135–49. https://doi.org/10.1016/j.jcp.2010.08.027.
[51] Asle Zaeem M, El Kadiri H, Mesarovic SD, Horstemeyer MF, Wang PT. Effect of the Compositional Strain on the Diffusive Interface Thickness and on the Phase Transformation in a Phase-Field Model for Binary Alloys. J Phase Equilibria Diffus 2011;32:302–8. https://doi.org/10.1007/s11669-011-9905-y.
[52] Zaeem MA, Mesarovic SD. Morphological instabilities in thin films: Evolution maps. Comput Mater Sci 2011;50:1030–6. https://doi.org/10.1016/j.commatsci.2010.10.043.
[53] Wang Y, Khachaturyan AG. Three-dimensional field model and computer modeling of martensitic transformations. Acta Mater 1997;45:759–73. https://doi.org/10.1016/S1359-6454(96)00180-2.
[54] Chen L-Q. Phase-Field Models for Microstructure Evolution. Annu Rev Mater Res 2002;32:113–40. https://doi.org/10.1146/annurev.matsci.32.112001.132041.
[55] Mamivand M, Zaeem MA, El Kadiri H. A review on phase field modeling of martensitic phase transformation. Comput Mater Sci 2013;77:304–11. https://doi.org/10.1016/j.commatsci.2013.04.059.
[56] Anderson PW, Blount EI. Symmetry Considerations on Martensitic Transformations: "Ferroelectric" Metals? Phys Rev Lett 1965;14:217–9. https://doi.org/10.1103/PhysRevLett.14.217.
[57] Axe JD, Yamada Y. Cubic-tetragonal elastic phase transformations in solids. Phys Rev B 1981;24:2567–9. https://doi.org/10.1103/PhysRevB.24.2567.
[58] Cui Y-W, Koyama T, Ohnuma I, Oikawa K, Kainuma R, Ishida K. Simulation of hexagonal–orthorhombic phase transformation in polycrystals. Acta Mater 2007;55:233–41. https://doi.org/10.1016/j.actamat.2006.07.026.
[59] Wen YH, Wang Y, Chen LQ. Phase-field simulation of domain structure evolution during a coherent hexagonal-to-orthorhombic transformation. Philos Mag A 2000;80:1967–82. https://doi.org/10.1080/01418610008212146.
[60] Wen YH, Wang Y, Chen LQ. Effect of elastic interaction on the formation of a complex multi-domain microstructural pattern during a coherent hexagonal to orthorhombic transformation. Acta Mater 1999;47:4375–86. https://doi.org/10.1016/S1359-6454(99)00247-5.
[61] Shchyglo O, Salman U, Finel A. Martensitic phase transformations in Ni–Ti-based shape memory alloys: The Landau theory. Acta Mater 2012;60:6784–92. https://doi.org/10.1016/j.actamat.2012.08.056.
[62] Zhu WZ. Grain size dependence of the transformation temperature of tetragonal to monoclinic phase in ZrO2(Y2O3) ceramics. Ceram Int 1996;22:389–95. https://doi.org/10.1016/0272-8842(95)00120-4.
[63] Garvie RC. Thermodynamic analysis of the tetragonal to monoclinic transformation in a constrained zirconia microcrystal. J Mater Sci 1985;20:3479–86. https://doi.org/10.1007/BF01113754.
[64] Mamivand M, Asle Zaeem M, El Kadiri H, Chen L-Q. Phase field modeling of the tetragonal-to-monoclinic phase transformation in zirconia. Acta Mater 2013;61:5223–35. https://doi.org/10.1016/J.ACTAMAT.2013.05.015.
[65] Miehe C, Hofacker M, Welschinger F. A phase field model for rate-independent crack propagation: Robust algorithmic implementation based on operator splits. Comput Methods Appl Mech Eng 2010;199:2765–78. https://doi.org/10.1016/j.cma.2010.04.011.

[66] Miehe C, Welschinger F, Hofacker M. Thermodynamically consistent phase-field models of fracture: Variational principles and multi-field FE implementations. Int J Numer Methods Eng 2010;83:1273–311. https://doi.org/10.1002/nme.2861.
[67] Borden MJ, Verhoosel C V., Scott MA, Hughes TJR, Landis CM. A phase-field description of dynamic brittle fracture. Comput Methods Appl Mech Eng 2012;217:77–95. https://doi.org/10.1016/j.cma.2012.01.008.
[68] Hesch C, Weinberg K. Thermodynamically consistent algorithms for a finite-deformation phase-field approach to fracture. Int J Numer Methods Eng 2014;99:906–24. https://doi.org/10.1002/nme.4709.
[69] Rabczuk T. Computational Methods for Fracture in Brittle and Quasi-Brittle Solids: State-of-the-Art Review and Future Perspectives. ISRN Appl Math 2013;2013. https://doi.org/10.1155/2013/849231.
[70] Mamivand M, Asle Zaeem M, El Kadiri H. Effect of variant strain accommodation on the three-dimensional microstructure formation during martensitic transformation: Application to zirconia. Acta Mater 2015;87:45–55. https://doi.org/10.1016/j.actamat.2014.12.036.
[71] Hayakawa M, Adachi K, Oka M. Crystallographic analysis of the monoclinic herringbone structure in an arc-melted ZrO2-2 mol% Y2O3 alloy. Acta Metall Mater 1990;38:1753–9. https://doi.org/https://doi.org/10.1016/0956-7151(90)90017-B.
[72] Hayakawa M, Kuntani N, Oka M. Structural study on the tetragonal to monoclinic transformation in arc-melted ZrO2-2mol.%Y2O3—I. Experimental observations. Acta Metall 1989;37:2223–8. https://doi.org/https://doi.org/10.1016/0001-6160(89)90148-X.
[73] LANDAU LD. Collected Papers of L.D. Landau. Oxford: Pergamon Press; 1965.
[74] Landau LD, Lifshitz EM. Statistical physics. Oxford: Pergamon Press; 1980.
[75] Cahn JW, Hilliard JE. Free Energy of a Nonuniform System. I. Interfacial Free Energy. J Chem Phys 1958;28:258–67. https://doi.org/10.1063/1.1744102.
[76] Khachaturyan A. Theory of structural transformations in solids. 1983.
[77] Francfort GA, Marigo J-J. Revisiting brittle fracture as an energy minimization problem. J Mech Phys Solids 1998;46:1319–42. https://doi.org/10.1016/S0022-5096(98)00034-9.
[78] Griffith AA. VI. The phenomena of rupture and flow in solids. Philos Trans R Soc London Ser A, Contain Pap a Math or Phys Character 1921;221:163–98.
[79] Amor H, Marigo JJ, Maurini C. Regularized formulation of the variational brittle fracture with unilateral contact: numerical experiments. J Mech Phys Solids 2009;57:1209–29.
[80] Simha NK. Twin and habit plane microstructures due to the tetragonal to monoclinic transformation of zirconia. J Mech Phys Solids 1997;45:261–92. https://doi.org/10.1016/S0022-5096(96)00074-9.
[81] Bansal G., Heuer A. On a martensitic phase transformation in zirconia (ZrO2)—II. Crystallographic aspects. Acta Metall 1974;22:409–17. https://doi.org/10.1016/0001-6160(74)90093-5.
[82] Bansal G., Heuer A. On a martensitic phase transformation in zirconia (ZrO2)—I. Metallographic evidence. Acta Metall 1972;20:1281–9. https://doi.org/10.1016/0001-6160(72)90059-4.
[83] Artemev A, Wang Y, Khachaturyan A. Three-dimensional phase field model and simulation of martensitic transformation in multilayer systems under applied stresses. Acta Mater 2000;48:2503–18. https://doi.org/10.1016/S1359-6454(00)00071-9.